Improved crossflow transition predictions for the one-equation γ transition model

Ginevra Rubino, Michel Visonneau

Improved Crossflow Transition Predictions for the one-equation γ transition model

Ginevra Rubino[a,*], Michel Visonneau[a],

[a]*Ecole Centrale de Nantes, CNRS, LHEEA, Nantes, 44321, France*

Abstract

A variant of the local correlation-based transition model (LCTM) γ is presented to account for the prediction of transition due to stationary crossflow instabilities. The presented $Tc1$ crossflow criterion is a local approximation of the well-known C1 criterion by Arnal (1984), evaluated locally through auxiliary functions expressed by the solution of the Falkner-Skan-Cooke (FSC) equations. The criterion, originally proposed by Menter & Smirnov (2014), uses the wall-normal directional change of the normalized vorticity as indicator of the crossflow strength. Hereafter, an original calibration FSC-based of Menter & Smirnov criterion is proposed. A local approximation of the sweep angle is included in order to achieve better results on non-wing-like geometries. The capability of this model variant to predict stationary crossflow transition is therefore discussed. A validation study is presented using experimental data on the 6:1 prolate spheroid and the sickle wing.

Keywords: RANS, Transition Modeling, Stationary Crossflow, Falkner-Skan-Cooke, γ model

1. Introduction

Nowadays understanding, predicting and controlling laminar-to-turbulence transition is one of the biggest challenges in Computational Fluid Dynamics (CFD). There are several practical applications that deal with low/moderate Reynolds numbers: aerial and marine unmanned vehicles, small submarines, but also wind

*Corresponding author

Email addresses: ginevra.rubino@ec-nantes.fr (Ginevra Rubino), michel.visonneau@ec-nantes.fr (Michel Visonneau)

turbines. For these applications transitional effects are important, if not dominant, and Reynolds averaged Navier-Stokes (RANS) turbulence models fail to predict them. In the last decade, the local-correlation transition model (LCTM) concept has known a huge success. The RANS transition models $\gamma - Re_\theta$, proposed by Menter & Langtry, [1], and γ by Menter *et al.*, [2], are today widely spread. They are preferred in practical applications to Direct Numerical Simulations (DNS) and Large Eddy Simulations (LES) approaches, because of the reduced computational costs. The aim of these RANS transition models is not to describe the transition physics, but rather to identify the different regions of the flow and to predict accurately the transition location. All the physics is contained in empirical correlations, that account for a specific transition mechanism. $\gamma - Re_\theta$ model, officially published in 2012, is based on the solution of two transport equations: one for the intermittency γ and one for the momentum thickness Reynolds number $\overline{Re_{\theta_t}}$. The quantity γ is used to turn on the production of turbulence kinetic energy in the boundary layer downstream the transition onset location. The equation for $\overline{Re_{\theta_t}}$ is needed to transport non-local information, namely the empirical momentum thickness Reynolds number Re_{θ_t}, from the free-stream inside the boundary layer. The solution of this second transport equation, $\overline{Re_{\theta_t}}$, appears in the definition of the critical momentum thickness Reynolds number, Re_{θ_c}. The latter is required in the empirical correlation that triggers the production of intermittency in the boundary layer.

The one-equation local correlation γ transition model was proposed in 2015 as a drastic simplification of $\gamma - Re_\theta$ model. The transport equations are reduced from two to one and the critical momentum thickness Reynolds number is computed through a fully local empirical correlation.

Within the NATO AVT-313 “Incompressible Laminar-to-Turbulent Flow Transition Study” collaboration group, $\gamma - Re_\theta$ and γ models performances have been tested on several configurations, both two- and three-dimensional. During these studies, it was observed that the two models perform very similarly in terms of transition predictions. Nevertheless, the one-equation γ model was found easier and faster to converge compared to $\gamma - Re_\theta$ (see Lopes, [3], Rubino, [4]). For this reason, in the present discussion attention is focused on the one-equation γ model and its extension to crossflow transition predictions.

Indeed, as originally presented, both $\gamma - Re_\theta$ and γ models only accounted for bypass and streamwise natural transition, as due to Tollmien-Schlichting (T-S) waves. In the last six years, different research groups have devoted their effort to the definition of a criterion to account for transition due to stationary crossflow waves (CF). These are the dominant instabilities modes on three-dimensional configurations operating in very low free-stream turbulence environments.

An empirical correlation that accounts for crossflow transition should be a function of the multiple pa-

rameters that play a role in the process: the pressure gradient in the streamwise direction, the Reynolds number (based on the boundary layer thickness), and the crossflow strength. Turbulence intensity and surface roughness also play a decisive role, but are often not accounted for. The majority of the crossflow criteria in literature uses the helicity $He = \overrightarrow{u} \cdot (\nabla \times \overrightarrow{u})$ as a measure of the crossflow strength. Its use was first proposed by Muëller & Herbst, [5], then by Langtry *et al.*, [6]. Both Muëller *et al.* and Langtry *et al.* CF extensions were thought to be coupled to $\gamma - Re_\theta$ model, involving the modification of the second transport equation for $\overline{Re_{\theta_t}}$. Therefore, their approaches cannot be directly used within the one-equation γ model formulation.

Grabe *et al.*, [7], also proposed an helicity-based crossflow criterion for $\gamma - Re_\theta$. The latter crossflow model, differently from the two variants mentioned above, envisages the modification of the onset function of the production term in the transport equation for the intermittency γ. This helicity-based crossflow criterion is calibrated on a numerical database constructed considering the experimental results on the ONERA D airfoil from Schmitt *et al.*, [8], and in ONERA/CERT/DERAT, [9], the results on the infinite-swept NLF (2)-0415 wing from Dagenhart *et al.*, [10], but also on the 3D 6:1 Prolate Spheroid from Kreplin, [11].

A different criterion to account for stationary crossflow transition is the one proposed by Menter & Smirnov, [12]. This is the so-called $Tc1$ crossflow criterion and it is a local reconstruction of the C1 criterion of Daniel Arnal, [13]. Arnal's C1 criterion is based on the crossflow Reynolds number $Re_{\delta 2}$:

$$Re_{\delta_2} = \frac{U_{1_e}\delta_2}{\nu} \text{ where } \delta_2 = -\int_0^\infty \frac{W_1}{U_{1_e}} dy, \tag{1}$$

where U_1 and W_1 are the streamwise and crosswise velocity components. $U_{1_e} = \sqrt{(U_e^2 + W_e^2)}$ is the velocity at the edge of the boundary layer. The C1 crossflow criterion reads as:

$$\frac{Re_{\delta 2}}{Re_{\delta 2t}} = 1, \tag{2}$$

where the Reynolds number value at the transition location, $Re_{\delta 2t}$, is not unique, but it depends on the longitudinal shape factor H_{12}. It is defined as:

$$Re_{\delta_{2t}} = \begin{cases} \frac{300}{\pi} \arctan\left(\frac{0.106}{(H_{12}-2.3)^{2.052}}\right), \text{ for } 2.3 < H_{12} \leqslant 2.7, \\ 150, \text{ for } H_{12} \leqslant 2.3. \end{cases} \tag{3}$$

The C1 criterion is empirically-based on the experimental results at low Tu from Poll, [14], around a cylinder of large diameter, Boltz *et al.*, [15], around NACA64$_2$ A 015 symmetric profile, and on the measurements around the ONERA D profile by Schmitt *et al.* and at ONERA/CERT/DERAT.

The $Tc1$ local approximation proposed by Menter & Smirnov uses the wall-normal directional change of the normalized vorticity vector, hereafter defined Ψ, as crossflow strength indicator. This quantity represents a measure of the three-dimensionality of the boundary layer. The quantity Ψ enters the critical crosswise Reynolds-number ratio of Eq.(2), which is evaluated locally through auxiliary functions expressed by the solution of the Falkner-Skan-Cooke (FSC) equations. The FSC are an extension of two-dimensional laminar boundary layer Falkner-Skan equations by considering the spanwise velocity component for a flow over an infinitely yawed wedge, i.e. the gradients in the spanwise directions are zero, at zero angle attack, Cooke, [16]. In Menter & Smirnov paper, the Tc1 criterion is used in conjunction with γ model, modifying the production term in the transport equation for the intermittency.

In this context, it is opted to pursue this research using the FSC-based $Tc1$ criterion, rather than the helicity-based criterion by Grabe *et al.* , as possible crossflow variant of the one-equation γ model. The rationale behind this choice is that a FSC-based calibration widens the "room of maneuvers" for model/code developers with respect to a calibration based on experimental databases reconstructed numerically. The use of an FSC framework allows to introduce more physics in the correlations used to trigger the transition process and to better understand a model behavior in default of detailed experimental data for transitional flows.

In the specific case of the $Tc1$ crossflow criterion, it was observed that this criterion, as originally formulated by Menter & Smirnov, did not perform well only on non-wing-like geometries. Therefore, in order to improve the $Tc1$ performance, an original re-calibration based on FSC velocity profiles is proposed to extend its range of application to more complex 3D geometries. The details of the re-calibration are given in this paper, that includes the following sections: description of the mathematical formulation of the one-equation γ model, introduction of the FSC equations, the detailed steps of the proposed original re-calibration. Finally, the numerical results obtained with the re-calibrated $Tc1$ criterion are discussed for two different three-dimensional configurations, exhibiting strengths and weaknesses of the proposed approach.

γ model with the $Tc1$ crossflow extension was implemented in the in-house ISIS-CFD solver, whose main features are described below.

2. ISIS-CFD AT A GLANCE

The solver ISIS-CFD, available as a part of the FINE™/Marine computing suite distributed by Cadence Design Systems, Inc., is an incompressible multiphase unsteady Reynolds-averaged Navier-Stokes (URANS) solver mainly devoted to marine hydrodynamics. It is based on a fully-unstructured (face-based) finite volume discretization with specific functionalities needed for multiphase flows and industrial applications, see Queutey & Visonneau, [17], Leroyer & Visonneau, [18], Wackers *et al.*, [19] and [20]. The method features several sophisticated turbulence models: apart from the classical two-equation k-ϵ and k-ω models, the anisotropic two-equation Explicit Algebraic Reynolds Stress Model (EARSM), as well as Reynolds Stress Transport Models (SSG/LRR). All models are available with wall-function or low-Reynolds near wall formulations. Hybrid RANS/LES turbulence models based on Detached Eddy Simulation (DES-SST, DDES-SST, IDDES) are also implemented and have been validated on automotive flows characterized by large separations, see Guilmineau *et al.*, [21]. The flow solver is combined with the mesh generator HEXPRESS^{TM}, which generates full hexaedral unstructured meshes.

The simulations presented in the discussion are for single fluid steady flows. Convective fluxes of transition, turbulence and momentum equations are discretized using AVLSMART scheme, a NVD diagram discretization scheme, based on the third-order QUICK scheme, Leonard, [22].

The following section is devoted to γ transition model formulation, as originally published by Menter *et al.*

3. One-equation γ transition model

The one transport equation for γ reads as:

$$\frac{\partial(\rho\gamma)}{\partial t} + \frac{\partial(\rho u_j \gamma)}{\partial x_j} = P_\gamma - E_\gamma + \frac{\partial}{\partial x_j}\left[\left(\mu + \frac{\mu_t}{\sigma_\gamma}\right)\frac{\partial \gamma}{\partial x_j}\right]. \tag{4}$$

The transition source term is constructed as:

$$P_\gamma = F_{\texttt{onset,2D}}[F_{\texttt{length,2D}}(\rho S(1-\gamma)\gamma)], \tag{5}$$

where $F_{\texttt{length,2D}}$ is constant and set to the value of 100. It represents the transition length and controls the strength of the intermittency production term. The activation of the latter is controlled by the function

$F_{\texttt{onset,2D}}$, built as:

$$F_{\texttt{onset,2D-1}} = \frac{Re_V}{2.2Re_{\theta_c}}, \tag{6}$$

$$F_{\texttt{onset,2D-2}} = \min(F_{\texttt{onset,2D-1}}, 2.0), \tag{7}$$

$$F_{\texttt{onset,2D-3}} = \max\left(1 - \left(\frac{R_T}{3.5}\right)^3, 0\right), \tag{8}$$

$$F_{\texttt{onset,2D}} = \max(F_{\texttt{onset,2D-2}} - F_{\texttt{onset,2D-3}}, 0), \tag{9}$$

where $Re_V = \frac{\rho S y^2}{\mu}$ is the vorticity Reynolds number. Re_{θ_c} is the critical momentum thickness Reynolds number, at which the instabilities are amplified in the boundary layer. $R_T = \nu_t/\nu$ is the eddy viscosity ratio. The relaminarization/destruction term depends on the magnitude of the absolute vorticity rate and it is defined as:

$$E_\gamma = c_{a2}\rho\Omega\gamma F_{\text{turb}}(c_{e2}\gamma - 1). \tag{10}$$

$F_{\texttt{turb}}$ deactivates the destruction term outside the boundary layer and it is given by:

$$F_{\text{turb}} = e^{-\left(\frac{R_T}{2}\right)^4}. \tag{11}$$

The model constants obtained by numerical calibration are :

$$c_{e2} = 50, \qquad c_{a2} = 0.06, \qquad \sigma_\gamma = 1. \tag{12}$$

The boundary conditions for γ are zero normal flux at the wall and equal to one at the inlet. The constant c_{e2}, Eq.(12), controls the lower limit of γ, i.e. the value at which the destruction term E_γ in Eq.(10) changes sign. The value $c_{e2} = 50$ enforces $\gamma = 1/c_{e2} = 0.02$ in the viscous sub-layer down to the wall. Re_{θ_c} is an empirical correlation and it is function of the local turbulence intensity Tu_L and pressure gradient parameter, $\lambda_{\theta,L}$. The turbulence intensity within the boundary layer is expressed as:

$$Tu_L = \min\left(100\frac{\sqrt{2k/3}}{\omega y}, 100\right). \tag{13}$$

The pressure gradient parameter λ_θ commonly used in empirical correlations is given by:

$$\lambda_\theta = -\frac{\theta^2}{\mu}\frac{1}{U}\frac{dP}{ds} = \frac{\theta^2}{\nu}\frac{dU}{ds}, \tag{14}$$

where $\frac{dU}{ds}$ is the derivative of the velocity in the streamwise direction at the edge of the boundary layer. For the flow on a flat plate, using the incompressibility constraint, Eq.(14) can be expressed as:

$$\lambda_\theta = \frac{\theta^2}{\nu}\frac{du}{dx} = -\frac{\theta^2}{\nu}\frac{d\mathrm{v}}{dy}, \tag{15}$$

where v and y are the wall-normal velocity component and coordinate in the free-stream, respectively. For a generic geometry, given the wall-normal velocity component v of the velocity vector $\overrightarrow{u}$, $\frac{d\mathrm{v}}{dy}$ can be expressed as:

$$\frac{d\mathrm{v}}{dy} \equiv \nabla(\overrightarrow{n}\cdot\overrightarrow{u})\cdot\overrightarrow{n}. \tag{16}$$

The quantity $\frac{d\mathrm{v}}{dy}$ is used in this formulation as an indicator within the boundary layer of the pressure gradient imposed from the free-stream. In order to express λ_θ locally, the momentum thickness θ is replaced by the wall distance y. The transition model is built to activate close to the center of the boundary layer and at this location, given the boundary layer thickness δ, $y = \frac{\delta}{2} \sim \theta$. Thus, y gives a proper scaling of θ inside the boundary layer. Finally, the local expression of pressure gradient parameter is expressed by:

$$\lambda^*_{\theta,L} = -7.57\cdot 10^{-3}\frac{d\mathrm{v}}{dy}\frac{y^2}{\nu} + 0.0128. \tag{17}$$

The scaling coefficients for $\lambda^*_{\theta,L}$ in Eq.(17) are obtained such that in the middle of the boundary layer $\lambda^*_{\theta,L}$ well approximates λ_θ obtained using the Falkner-Skan profiles. The constant 0.0128 is added in Eq.(17) in order to account for the fact that $\frac{d\mathrm{v}}{dy}$ is not zero in the middle of the boundary layer for zero pressure gradient flows ($\beta = \lambda_\theta = 0$), due to the growth of the boundary layer. The local pressure gradient parameter that enters the empirical correlation has to bounded for numerical reasons, resulting in the final formulation:

$$\lambda_{\theta,L} = \min(\max(\lambda^*_{\theta,L}, -1), 1). \tag{18}$$

The empirical correlation is finally expressed as follows:

$$Re_{\theta_c}(Tu_L, \lambda_{\theta,L}) = C_{TU1} + C_{TU2} * e^{-C_{TU3}Tu_L F_{PG}(\lambda_{\theta,L})}, \tag{19}$$

where the constants are:

$$C_{TU1} = 100, \qquad C_{TU2} = 1000, \qquad C_{TU3} = 1. \tag{20}$$

F_{PG} in Eq.(19) is built from the empirical function F^*_{PG}, calibrated on a series of Falkner-Skan profiles. The latter is defined as:

$$F^*_{PG}(\lambda_{\theta,L}) = \begin{cases} \min(1 + C_{PG1}\lambda_{\theta,L}, C^{\lim}_{PG1}) & \text{for } \lambda_{\theta,L} \geqslant 0 \\ \min(1 + C_{PG2}\lambda_{\theta,L} + C_{PG3}\min[\lambda_{\theta,L} + 0.0681, 0], C^{\lim}_{PG2}) & \text{for } \lambda_{\theta,L} < 0 \end{cases} \tag{21}$$

The constants are:

$$C_{PG1} = 14.68, \quad C_{PG2} = -7.34, \quad C_{PG3} = 0.0, \tag{22}$$

$$C^{\lim}_{PG1} = 1.5, \quad C^{\lim}_{PG2} = 3.0. \tag{23}$$

Finally, F_{PG} is given by:

$$F_{PG} = \max(F^*_{PG}, 0), \tag{24}$$

in order to avoid negative values. γ model interacts only with the turbulence kinetic energy k transport equation of the $k-\omega$ SST turbulence model 2003 version by Menter *et al.*, [23]. The production and destruction terms of k are modified as follows:

$$\frac{\partial(\rho k)}{\partial t} + \frac{\partial(\rho u_j k)}{\partial x_j} = P'_k + P^{\lim}_k - D'_k + \frac{\partial}{\partial x_j}\left[\left(\mu + \sigma_k \mu_t\right)\frac{\partial k}{\partial x_j}\right], \tag{25}$$

The primary production term P'_k is defined as:

$$P'_k = \gamma P_k \tag{26}$$

while, the destruction term is given by:

$$D'_k = \max(\gamma, 0.1) \cdot D_k. \tag{27}$$

D_k in Eq.(27) comes from the original $k-\omega$ SST (2003) turbulence model formulation. P_k in Eq.(26) is computed using Kato-Launder modification, [24], in order to reduce the excessive production of turbulence kinetic energy in regions with large normal strain. The additional production term $P^{\lim}_k$ accounts for separation-induced transition and it is defined as follows:

$$P^{\lim}_k = 5C_k(\max(\gamma - 0.2, 0))(1-\gamma)F^{\lim}_{\text{on}}(\max(3C_{SEP}\mu - \mu_t, 0))S\Omega, \tag{28}$$

where

$$F_{\text{on}}^{\text{lim}} = \min\left(\max\left(\frac{Re_V}{2.2 \cdot 1100} - 1, 0\right), 3\right), \tag{29}$$

$$C_k = 1.0, \qquad C_{SEP} = 1.0. \tag{30}$$

The equation for ω remains unchanged:

$$\frac{\partial(\rho\omega)}{\partial t} + \frac{\partial}{\partial x_j}\left(\rho U_j \omega - (\mu + \sigma_\omega \mu_t)\frac{\partial \omega}{\partial x_j}\right) = \gamma\rho\Omega^2 - \beta\rho\omega^2 + 2(1 - F_1)\frac{\rho\sigma_{\omega 2}}{\omega}\frac{\partial \omega}{\partial x_j}\frac{\partial k}{\partial x_j}. \tag{31}$$

The blending function between $k - \omega$ and $k - \epsilon$ formulations, F_1, is reformulated as:

$$F_1 = \max(F_{1orig}, F_3), \tag{32}$$

$$F_3 = e^{(\frac{R_y}{120})^8}, \; R_y = \frac{\rho y \sqrt{k}}{\mu}, \tag{33}$$

where F_{1orig} is the original function of $k - \omega$ SST model:

$$F_1 = \tanh\left(\left[\min\left\{\max\left\{2\frac{\sqrt{k}}{0.09 d\omega}, 500\frac{\mu}{\rho d^2 \omega}\right\}, \frac{4\rho\sigma_{\omega 2} k}{CD_{k\omega} d^2}\right\}\right]^4\right). \tag{34}$$

The transition models equations, as presented above, account for bypass and streamwise transition, either due to T-S waves or separation-induced. The present study aims to incorporate in the model formulation an empirical correlation that accounts for instabilities amplifying in the crosswise direction. The crossflow criterion is discussed upon the introduction of Falkner-Skan-Cooke equations in the following section.

4. Falkner-Skan-Cooke Equations

In Fig.(1), an infinite swept wing geometry is presented. Two different coordinate systems can be defined: the wing attached one, where x is aligned with the chordwise direction, and the second reference system, with x_1 aligned with the external inviscid streamlines. The three-dimensional boundary layer equations

system for the infinite swept wing, where the derivative along the span is zero $\left(\frac{\partial}{\partial z} = 0\right)$, reduces to:

$$\frac{\partial U}{\partial x} + \frac{\partial V}{\partial y} = 0, \tag{35}$$

$$U\frac{\partial U}{\partial x} + V\frac{\partial U}{\partial y} = U_e\frac{dU_e}{dx} + \nu\frac{\partial^2 U}{\partial y^2}, \tag{36}$$

$$U\frac{\partial W}{\partial x} + V\frac{\partial W}{\partial y} = \nu\frac{\partial^2 W}{\partial y^2}. \tag{37}$$

with boundary conditions:

$$U = V = W = 0 \text{ at } y = 0, \tag{38}$$

$$U \to U_e \text{ and } W \to W_e \text{ as } y \to \infty. \tag{39}$$

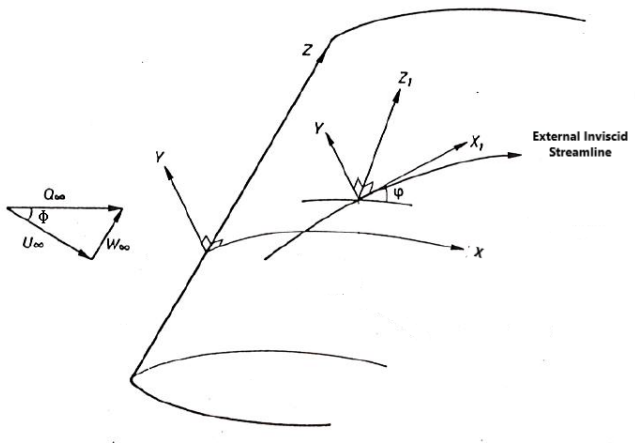

Figure 1: Infinite swept wing notations used to formulate the FSC equations.

It is supposed that the inviscid chordwise velocity at the boundary layer edge U_e follows a potential law over the coordinate normal to the leading edge x and that the spanwise velocity (parallel to the leading edge) W_e is constant. The two components can be written as:

$$U_e \sim U_\infty\left(\frac{x}{L}\right)^m, \tag{40}$$

$$W_e = const, \tag{41}$$

where L is the characteristic length and U_∞ is the free-stream longitudinal velocity. m is the streamwise

pressure gradient and it is expressed as:

$$m = \frac{x}{U_e}\frac{dU_e}{dx}. \tag{42}$$

Once defined the Blasius similarity variable η as:

$$\eta = y\sqrt{\frac{U_\infty(m+1)}{2\nu L}}\left(\frac{x}{L}\right)^{(m-1)/2}, \tag{43}$$

and introduced the stream function Ψ^*:

$$\Psi^* = \sqrt{\frac{2U_\infty \nu L}{m+1}}\left(\frac{x}{L}\right)^{(m+1)/2} f(\eta), \tag{44}$$

with $U = \frac{\partial \Psi^*}{\partial y}$, $V = -\frac{\partial \Psi^*}{\partial x}$, the continuity equation is automatically satisfied. Eq.(36) becomes:

$$f''' + ff'' + \beta(1 - f'^2) = 0, \tag{45}$$

where β is the Hartree parameter associated to m by the relation:

$$\beta = \frac{2m}{m+1}. \tag{46}$$

The dash $'$ in Eq.(45) denotes the differentiation with respect to η. Finally, given $W = W_e g(\eta)$, Eq.(37) becomes:

$$g'' + fg' = 0. \tag{47}$$

The system of equations in Eq.(45)-(47) are the Falkner-Skan-Cooke equations. The corresponding boundary conditions are:

$$f, f', g \to 0 \text{ for } \eta \to 0, \tag{48}$$

$$f', g \to 1 \text{ for } \eta \to \infty. \tag{49}$$

The solutions f' and g can be combined into the dimensionless streamwise and crosswise velocity components, non-dimensionalized with respect to the velocity magnitude at the edge of the boundary layer U_{1_e}.

Their expression is given by:

$$U_1/U_{1_e} = f' \cos(\phi)^2 + g \sin(\phi)^2, \tag{50}$$

$$W_1/U_{1_e} = (g - f') \cos(\phi) \sin(\phi). \tag{51}$$

In Eq.(50) and Eq.(51) ϕ is the sweep angle, i.e. the angle of the inviscid flow direction with respect to the chordwise direction at the edge of the boundary layer. It is constant along the wall normal height of the boundary layer. It is defined such that:

$$\tan(\phi) = \frac{W_e}{U_e}. \tag{52}$$

According to the definition in Eq.(51), $W_1 = 0$ for $\phi = 0°$ and $\phi = 90°$, but also for zero pressure gradient flows, $\beta = 0$, because $g - f' = 0$. The last condition does not occur in real physical flows, because crossflow velocity also exists for zero-pressure gradients three-dimensional flows.

5. Tc1 Criterion Calibration

The C1 criterion from Arnal of Eq.(2) can be rewritten in the form:

$$\frac{Re_{\delta_2}}{f(H_{12})150} = 1, \tag{53}$$

where $f(H_{12})150$ is the value of the crossflow Reynolds number $Re_{\delta_{2t}}$ at transition onset. Menter & Smirnov in [12] propose to split the C1 criterion in three different terms. The purpose is to identify and quantify each parameter that affects the crossflow transition onset. The C1 criterion can then be rewritten as:

$$\frac{Re_{\delta 2}}{f(H_{12})} \sim F(H_{12}) X Re_{\texttt{stream}}. \tag{54}$$

The function $F(H_{12}) = \frac{1}{f(H_{12})}$ takes into account the pressure gradient in the streamwise direction, X is a measure of the crossflow strength and $Re_{\texttt{stream}}$ is the Reynolds number relative to the streamwise velocity component. The latter is taken to be the maximum value of the vorticity Reynolds number in the boundary layer $Re_{V_{\max}}$. Based on Eq.(54), a local approximation of the C1 criterion, referred to as $Tc1$, is given by:

$$Tc1 = \frac{1}{150}\Big[G \cdot \Psi \cdot Re_{V_{\max}}\Big], \tag{55}$$

where

$$\Psi \sim X = \frac{Re_{\delta 2}}{Re_{V_{\max}}}, \tag{56}$$

$$G \sim F(H_{12}) = \frac{1}{f(H_{12})}. \tag{57}$$

The $Tc1$ criterion, as formulated in Eq.(55), is mathematically equivalent to Arnal's C1 criterion.

The function Ψ approximates the ratio of the crossflow to the streamwise strength. As proposed by Menter & Smirnov, it is constructed using the wall-normal change of the normalized vorticity. This quantity describes the three dimensionality of the boundary layer. Indeed, $\Psi = 0$ for 2D flows because $w = 0$, as well as all the derivatives in the spanwise direction z. Ψ is defined as:

$$\Psi = \mid \overrightarrow{\psi} \mid \cdot y, \tag{58}$$

where y is the wall normal distance. The components of the vector $\overrightarrow{\psi} = \{\psi_i\}$ are given by:

$$\psi_i = \frac{\partial \overline{\omega_i}}{\partial x_j} n_j, \text{ where } \overline{\omega_i} = \frac{\omega_i}{\mid \overrightarrow{\omega} \mid}. \tag{59}$$

The scalar quantity Ψ can be interpreted as an indicator of the crossflow strength being proportional to the local change of the flow angle.

The local approximation in Eq.(55) is evaluated using FSC solutions and it is used to develop a CFD crossflow criterion. An original re-calibration of $Tc1$ FSC-based is presented in the following discussion.

The FSC equations are solved in the parameter range:

$$0 < \beta \leq 1, \tag{60}$$

$$0° < \phi < 90°. \tag{61}$$

β is restricted to positive values, because crossflow instabilities occur for accelerated flow, in a favorable pressure gradient. $\beta = 1$ is the case of 90° wedge, i.e. the 2D stagnation flow, and it is the highest possible acceleration parameter. ϕ is the sweep angle as defined in Eq.(52). For the calibration, Ψ and all the local variables are evaluated at the location $\eta = \eta_{\max}$ in the wall-normal direction where $Tc1(\eta_{\max})$ reaches its maximum value. Within the FSC framework the quantity Ψ is approximated considering only the derivatives

with respect to the normal direction η. The vorticity components that exist in the FSC framework are:

$$\omega_x \sim \frac{\partial W_1/U_{1_e}}{\partial \eta}\frac{\partial \eta}{\partial y} = \left((g' - f'')\sin(\phi)\cos(\phi)\frac{\partial \eta}{\partial y}\right)\Big| U_{1_e}, \tag{62}$$

$$\omega_z \sim -\frac{\partial U_1/U_{1_e}}{\partial \eta}\frac{\partial \eta}{\partial y} = -\left(\left(f''\sin(\phi)^2 + g'\cos(\phi)^2\right)\frac{\partial \eta}{\partial y}\right)\Big| U_{1_e}. \tag{63}$$

The ratio $R(\beta,\phi) = \frac{a\Psi}{X}$ is shown in Fig.(2), where the constant a is set to 0.4 in order to match the two indicators Ψ and X for $\beta \to 0$. The maximum deviation of the two indicators ratio with respect to the targeted value of 1 is about 35%. Nevertheless, this deviation occurs at the corners of the domain and lies in the limits of the experimental correlation C1 from Arnal, i.e. deviation of the experimental results from the correlation $Re_{\delta_2 t}$. Therefore, Ψ fairly approximates the ratio X.

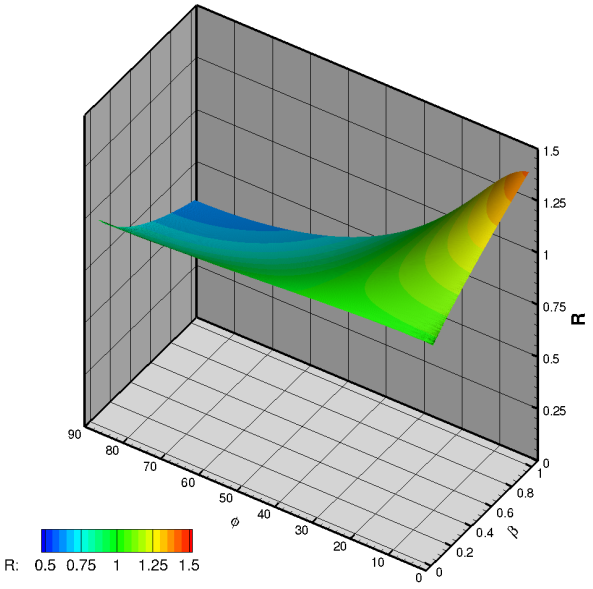

Figure 2: Crossflow indicators ratio $R(\beta,\phi) = 0.4\Psi/X$, as a function of the Hartree parameter, β, and the sweep angle, ϕ.

The principal complication arises from the introduction of the function $f(H_{12})$.

The ratio $R(\beta,\phi) = a'\Psi/(XF(H_{12}))$ is shown in Fig.(3), where the new constant $a' = 0.684$ is chosen in order to have a value of $R \sim 1$ for $\beta \to 0$. It can be noticed that, at the upper corners of the domain, the ratio R now significantly departs from the targeted value of 1. This discrepancy is unacceptable and needs a correction. Menter & Smirnov propose a one-parameter function G_{MS} as a correction of the ratio $R = 0.684\Psi/(XF(H_{12}))$. Nonetheless, their calibration was performed for sweep angles smaller than 60°, which is a very low limit for complex non-wing-like 3D geometries.

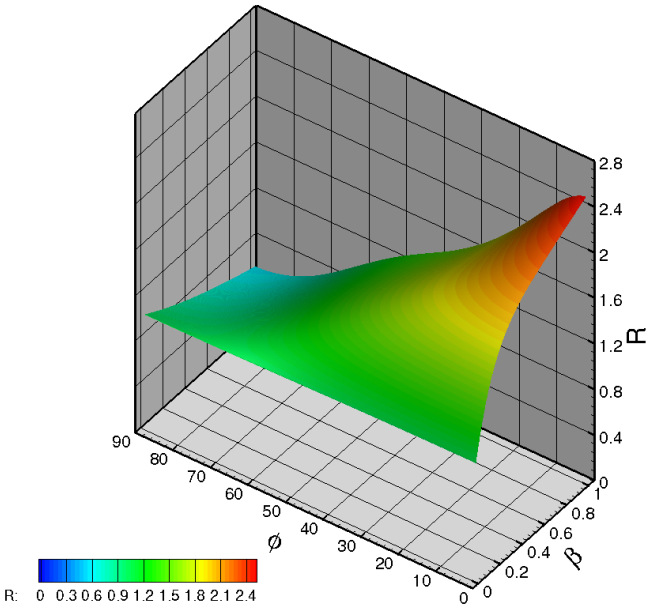

Figure 3: Ratio $R(\beta, \phi) = 0.684\Psi/(XF(H_{12}))$, as a function of the Hartree parameter, β, and the sweep angle, ϕ.

A possible strategy to achieve a proper fitting is to include in the local formulation of the $Tc1$ criterion a local version of the sweep angle ϕ, other than a local approximation of the Hartree parameter β. It is worthwhile to mention that the two independent FSC parameters, β and ϕ, are not known in the local formulation. β is included in the formulation through the pressure gradient parameter λ_θ, defined as:

$$\lambda_\theta = \frac{\theta^2}{\nu}\frac{dU_{1_e}}{dx} = \beta\left(\int_0^\infty \frac{U_1}{U_{1,e}}\left(1 - \frac{U_1}{U_{1,e}}\right)d\eta\right)^2. \tag{64}$$

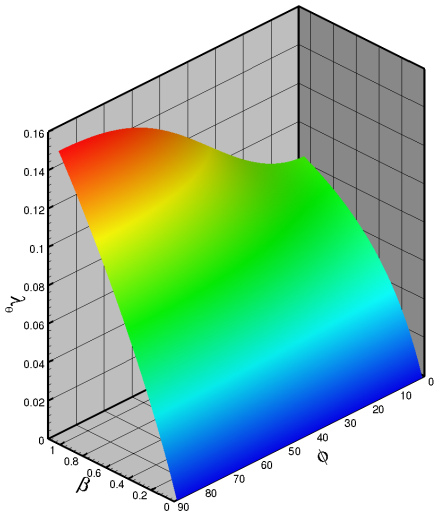

Figure 4: Pressure gradient parameter λ_θ plotted as a function of the Hartree parameter β and the sweep angle ϕ.

As shown in Fig.(4), λ_θ strongly depends on the sweep angle ϕ and this dependence needs to be accounted for within the crossflow transition criterion. For this reason, it is proposed to construct the pressure gradient parameter λ_θ as a two parameter function in ϕ and in the dimensionless quantity $\frac{dv}{dy}\frac{y^2}{\nu}$. The wall-normal derivative of v is defined as in Eq.(16). The new λ_θ for the crossflow inclusion is defined approximately at the middle of the boundary layer, where $y = \delta/2 \sim \theta$, as a 3rd order polynomial in the two variables $\frac{dv}{dy}\frac{y^2}{\nu}$ and ϕ. The fitted surface is obtained using a least squares method. The surface λ^*_{CF} is given by:

$$\begin{aligned}\lambda^*_{CF} =& 0.0473 - 0.0001338\,\phi - 0.02524\left(\frac{dv}{dy}\frac{y^2}{\nu}\right)\\ &+5.493e^{-6}\,\phi^2 - 2.148e^{-5}\,\phi\left(\frac{dv}{dy}\frac{y^2}{\nu}\right) + 0.001067\left(\frac{dv}{dy}\frac{y^2}{\nu}\right)^2\\ &-4.031e^{-8}\,\phi^3 - 2.81210^{-7}\,\phi^2\left(\frac{dv}{dy}\frac{y^2}{\nu}\right) + 1.053e^{-5}\,\phi\left(\frac{dv}{dy}\frac{y^2}{\nu}\right)^2\\ &+0.0002366\left(\frac{dv}{dy}\frac{y^2}{\nu}\right)^3.\end{aligned} \tag{65}$$

For numerical reasons, the λ_{CF} used in criterion has to be bounded. It is defined as:

$$\lambda_{CF} = \min\Big(\max\left(\lambda^*_{CF}, 0\right), 0.16\Big). \tag{66}$$

Then, the function G, in Eq.(55), that accounts for the streamwise pressure gradient, is constructed as the

surface $G = G(\lambda_{CF}, \phi)$. Its expression is given by:

$$\begin{aligned} G(\lambda_{CF}, \phi) =& 1.992 - 0.7328\ \phi - 0.00573\ \lambda_{CF} \\ &+0.02344\ \phi^2 - 0.1868\ \phi\ \lambda_{CF} - 0.08126\ \lambda_{CF}^2 \\ &+0.05222\ \phi^3 + 0.02332\ \phi^2\ \lambda_{CF} + 0.04903\ 10^{-5}\ \phi\ \lambda_{CF}^2 \\ &+0.03326\ \lambda_{CF}^3, \end{aligned} \tag{67}$$

where both λ_{CF} and ϕ are normalized with respect to their mean value and standard deviation. For the construction of the function G, λ_{CF} is evaluated at the position $\eta_{\max}$, where the $Tc1$ reaches its maximum. The new ratio $R = G\Psi/(XF(H_{12}))$ is plotted in Fig.(5) versus the two dependent variables λ_{CF} and ϕ. It can be observed that the benefit of introducing the definition of ϕ is a considerable reduction of the spread of the ratio R around the value of one, with a maximum deviation of less than 10%.

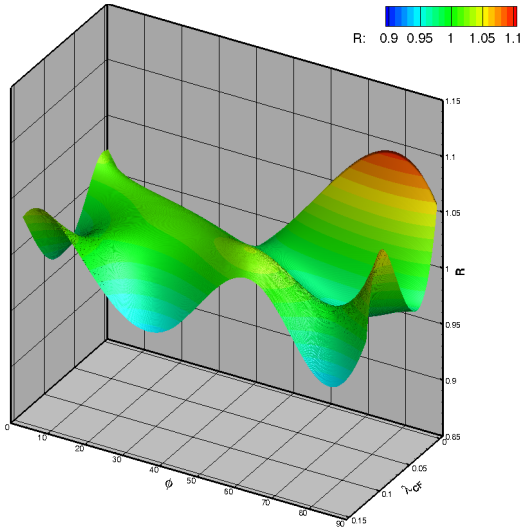

Figure 5: $R = G\Psi/(XF(H_{12}))$ vs the fitted pressure gradient parameter $\lambda_{CF} = \lambda_{CF}\left(\frac{d\nu}{dy}\frac{y^2}{\nu}, \phi\right)$ and the sweep angle ϕ.

The definition of ϕ as the angle between the external potential flow direction, U_{1_e}, aligned with the reference coordinate system (x_1, y, z_1), and the wing-attached reference system (x, y, z), is not CFD-compatible. Indeed, it would require the definition of the wing-attached reference system and the identification of the boundary layer edge. Hence, following Högberg & Henningson, [25], the sweep angle is defined with respect to the reference system (x_p, y, z_p), identified by the direction of the pressure gradient vector at each point, $(\overrightarrow{\nabla p})$, and the reference coordinate system (x, y, z), identified through the velocity vector $\overrightarrow{u} = (u, v, w)$. In this new coordinate system, x_p is aligned with the pressure gradient, y is normal to the surface, and z_p is

perpendicular to the plane (x_p, y), since, by FSC assumption, the pressure gradient is zero in the spanwise direction. A local sweep angle ϕ_L definition can be computed as in Choi *et al.*, [26], as follows:

$$\phi_L = \arccos\left(\frac{\overrightarrow{u}_{wt} \cdot \overrightarrow{(\nabla p)}_{wt}}{||\overrightarrow{u}_{wt}||||\overrightarrow{(\nabla p)}_{wt}||}\right), \ \phi_L = \min[\phi_L, \pi - \phi_L]. \tag{68}$$

$\overrightarrow{u}_{wt}$ and $\overrightarrow{(\nabla p)}_{wt}$ are the tangential projection at the wall of the local velocity vector and the pressure gradient. The use of the local velocity vector is an acceptable approximation, because the maximum value of the $Tc1$ criterion is reached close to the boundary layer edge, where ϕ_L recovers the original definition of ϕ of Eq.(52).

Galilean invariance. The approximation proposed for ϕ_L uses the local velocity vector and it makes γ model not Galilean invariant. In order to achieve a "weak Galilean invariant" formulation, such that the invariance with respect to Galilean transformations is preserved despite the use of the velocity vector, the local sweep angle is numerically implemented using the relative velocity vector $\overrightarrow{u}_{\texttt{rel}}$ defined as:

$$\overrightarrow{u}_{\texttt{rel}} = \overrightarrow{u} - \overrightarrow{u}_{\texttt{wall}}, \tag{69}$$

instead of the local velocity vector. This is a fair modification, when dealing with boundary-layer transition. In ISIS-CFD solver, the velocity at the wall is known throughout the simulation. From the beginning of the simulation, for each cell center, close to a no-slip wall, or a surface treated with wall functions, the face index of its correspondent point at the wall is stocked in a table. By "its correspondent point at the wall" is meant the point which minimizes the distance from the cell center to the wall. As in ISIS-CFD, the search of the point at the wall is a feature common to most of industrial codes, and it is performed independently of the use of a transition model. This implementation has its own limitations. Indeed, the research of the point at the wall might be troublesome at the junctions between multiple bodies with possibly different velocities, as the rotor blades of an helicopter.

A "strong Galilean invariant" formulation, that does not use explicitly the velocity or the streamlines direction, would require the discard of the sweep angle. Indeed, even if the local velocity vector is substituted by another variable, the dependence on the axes aligned with the velocity would be intrinsic and its use outside boundary layers can hardly be defended as Galilean invariant, as in its "strong" sense.

Implementation in ISIS-CFD solver. The derivative of the vorticity, which enters the $Tc1$ criterion through the indicator Ψ, is calculated as the Hessian of the local velocity vector. Each entrance of the Hessian

matrix is built through a least squares 3rd order accurate interpolation. The evaluation of the hessian of a scalar quantity at the center of the cell C_0 makes use of n points that provide the centers of the neighboring cells $C_{i=1,\dots,n}$. As a first set of neighbors cells $(C_1)_i$ the volumes which share a vertex with the cell C_0 are taken. As a second set of neighbors the volumes $(C_2)_i$ which share a face with $(C_1)_i$ are chosen. This approximation is fairly good for *2nd* derivatives calculated at the edge of the boundary layer, which is the region of interest.

The calculation of a *2nd* derivative within the boundary layer might be troubling and requires a mesh refined enough in both streamwise and spanwise directions. Nevertheless, these stringent requirements on the mesh refinement are the same demanded by the transition models for accurate predictions with negligible discretization error.

5.1. Inclusion of Tc1 Crossflow Criterion within γ formulation

The $Tc1$ criterion is further included in the γ formulation, modifying the $F_{\texttt{onset,2D}}$ function in the transport equation for the intermittency γ, Eq.(5). A new $F_{\texttt{onset},CF}$, that triggers the production of γ and based on the $Tc1$ criterion, is summed up to the $F_{\texttt{onset,2D}}$ function of the original formulation. $F_{\texttt{onset},CF}$ is defined as:

$$F_{\texttt{onset1},CF} = \frac{G\,\Psi\,Re_V}{c\;150}, \tag{70}$$

$$F_{\texttt{onset2},CF} = \min[\max(F_{\texttt{onset1},CF}, 0), 2], \tag{71}$$

$$F_{\texttt{onset3},CF} = \max(1 - (R_T/a)^3, 0), \tag{72}$$

$$F_{\texttt{onset},CF} = \max(F_{\texttt{onset2},CF} - F_{\texttt{onset3},CF}, 0), \tag{73}$$

$$a = 1.5,\; c = 0.6. \tag{74}$$

Through the proportionality constant c in Eq.(70), it is accounted for the difference between the critical crossflow Reynolds number, at which the intermittency starts to increase, and the crossflow Reynolds number at transition. The new $F_{\texttt{onset}}$ function that substitutes $F_{\texttt{onset},2D}$ in the transport equation for the intermittency γ, Eq.(5), is given by:

$$F_{\texttt{onset}} = F_{\texttt{length,2D}} F_{\texttt{onset},2D} + F_{\texttt{length},CF} F_{\texttt{onset},CF}, \tag{75}$$

where $F_{\texttt{length},CF} = 5$. The latter parameter has been set considering that crossflow instabilities develop on a longer length compared to T-S waves for which $F_{\texttt{length,2D}} = 100$. The constants, a and $F_{\texttt{length},CF}$, c were obtained from numerical calibration.

6. 3D Simulations

The present section is devoted to the analysis of the performance of $Tc1$ crossflow criterion for three-dimensional configurations. Predictions by the crossflow $Tc1$ model variant, hereafter referred to as $\gamma + CF$, are compared to results from the transition model without crossflow, indicated by the title γ, and experimental results. Two different geometrical configurations are considered: the 6:1 prolate spheroid at three different angles of attack, $\alpha = 5°, 15°, 30°$, and $Re = 6.5 \times 10^6$, and the sickle wing at $\alpha = -2.6°$, and $Re = 2.75 \times 10^6$. The inlet boundary conditions are imposed with respect to a targeted value of turbulence kinetic energy Tu recovered from the experimental data. The strategy to impose the boundary conditions is explained in the next section.

6.1. Inlet Boundary Conditions

Initial disturbances, their frequency and their amplitude are translated within the RANS framework in the value of turbulence intensity Tu, and eddy viscosity ν_t, that are imposed at the inlet. Tu quantifies the velocity fluctuations and it is defined as:

$$Tu = \sqrt{\frac{2k}{3}}/U, \tag{76}$$

where U is the velocity norm. ν_t is linked to the turbulence reference length L_{turb} by the relation:

$$\nu_t = TuU_{ref}L_{turb} = k/\omega. \tag{77}$$

Both quantities depend on the turbulence kinetic energy k and the turbulence frequency rate ω at the inlet, and on their free-decay ahead of the body. Indeed, in the free-stream, the destruction terms of the turbulence transport equations are active. The turbulence quantities undergo a decay that can have a strong impact on the numerical solution within the boundary layer, as discussed by Spalart & Rumsey, [27]. Free decay rates of turbulence quantities can be studied from the solution of the $k-\omega$ SST equations in the approaching flow field. The transport equations for k and ω for an incompressible and steady flow reduce to:

$$U_j\frac{\partial k}{\partial x_j} = \nu_t S^2 - \beta^*\omega k + \frac{\partial}{\partial x_i}\Big((\nu + \sigma_k\nu_t)\frac{\partial k}{\partial x_i}\Big), \tag{78}$$

$$U_j\frac{\partial \omega}{\partial x_j} = \gamma\Omega^2 - \beta\omega^2 + \frac{\partial}{\partial x_i}\Big((\nu + \sigma_\omega\nu_t)\frac{\partial \omega}{\partial x_i}\Big) + CD_{k\omega}, \tag{79}$$

where the constants are $\beta = 0.0828$ and $\beta^* = 0.09$. If the flow is uniform and aligned with x, neglecting the diffusion and cross-diffusion terms, the equations simplify to:

$$\frac{dk^*}{dx^*} = -\beta^* k^* \omega^*, \tag{80}$$

$$\frac{d\omega^*}{dx^*} = -\beta(\omega^*)^2. \tag{81}$$

The superscript * indicates the dimensionless variables, defined as $k^* = k/U_\infty^2$, $\omega^* = \omega L/U_\infty$, $\nu_t^* = k^*/\omega^*$, with $U = U_\infty$, and $x^* = x/L$. The analytical solutions of Eq.(80) and (81) are given by:

$$k^* = k_{in}^*(1 + \beta(x^* - x_{in}^*)\omega_{in}^*)^{\frac{-\beta^*}{\beta}}, \tag{82}$$

$$\omega^* = \omega_{in}^*(1 + \beta(x^* - x_{in}^*)\omega_{in}^*)^{-1}. \tag{83}$$

The solution for ν_t^* reads as:

$$\frac{\nu_t^*}{\nu} = \frac{\nu_{t_{in}}^*}{\nu}\Big[1 + \beta((x^* - x_{in}^*)\omega_{in}^*)\Big]^{\left(\frac{\beta^*}{\beta}-1\right)}. \tag{84}$$

The subscript $_{in}$ indicates the variable at the inlet of the computational domain. From Eq.(82), (83) and (84), it can be observed that the rate of the decay is exponential. ν_t^*/ν is the quantity which undergoes the decay at the slowest rate. Rewriting the specific turbulence dissipation rate ω_{in}^* as:

$$\omega_{in}^* = k_{in}^* \frac{\nu}{\nu_{t_{in}}^*} Re, \tag{85}$$

and substituting it in Eq.(82) and (84), it is observed that the decay depends on the Reynolds number and can be controlled through the eddy viscosity ratio. By increasing the eddy viscosity ratio at the inlet, the decay of k^* and ω^* can be contained. In order to limit the decay of turbulence quantities ahead of the body, a possible strategy is, therefore, to impose high values of eddy viscosity ratio R_T at the inlet. This method has to be used with care because, as discussed in Spalart & Rumsey, high values of eddy viscosity ratio can pollute the flow field in non-turbulent region.

Finally, to impose the initial conditions, specific values of eddy viscosity ratio, chosen by the CFD users, are specified at the inlet, in order to obtain the desired value of turbulence intensity close to the body. The latter should be recovered from the experiments, but it is not always an available information. The value of turbulence kinetic energy at the inlet k_{in} is then obtained from Eq.(82).

6.2. 6:1 Prolate Spheroid

The 6:1 prolate spheroid is a geometry commonly used both in hydrodynamic and aerodynamic, because it serves as simple surrogate for axisymmetric bodies as airplane fuselage and submarine hulls, as well as engine cowling on helicopters. The 6:1 prolate spheroid at incidence is one of the most investigated test cases, both experimentally and numerically, because it exhibits all the complex physics associated with crossflow transition and crossflow separation. For the validation of the numerical results here presented, it is referred to the experiments performed by Kreplin in 1985 at DLR, [11], that fully describe transition at the surface, through the measurements of wall shear stress magnitude and direction.

6.2.1. Experimental Set Up

Experiments were performed in the $3m \times 3m$ low speed wind tunnel at DLR Gottingen, around the 6:1 prolate spheroid of length of $2.4m$. Measurements at the surface were obtained using surface hot film probes: the wall shear stress magnitude is derived from the heat transfer rates of the films of each probe. The probes are positioned at 12 different stations along the longitudinal axis of the specimen. The magnitude of the wall shear stress τ_w is derived from the sum of the heat transfer rates of the films of each probes. A rough estimation of the error bound for the wall shear stress magnitude is given to be $\Delta\tau_w = \pm 20\%$. This high uncertainty is related to the fact that the hot-film probes were calibrated on flat tunnel wall for a 2D turbulent boundary layer, and, around the 6:1 prolate spheroid at incidence, the laminar region is quite extended.

Presented computations are run for the Reynolds number $Re = 6.5 \times 10^6$, for which transition occurs under the interaction of T-S and CF instabilities. For angles of attack higher than $\alpha = 5°$, zones of pure crossflow are observed in the middle of the inclined prolate spheroid and they become wider as the inclination is increased. Unfortunately, no specific indication on the free-stream conditions was given in the experimental report, but it is mentioned that Tu varies from 0.1% to 0.3% depending on the Reynolds number. Not knowing the free-stream Tu value is a big limitation, that does not allow to perform a rigorous validation exercise. Indeed, experimental conditions cannot be repeated with exactitude. For the presented exercise, the free-stream conditions are chosen in order to obtain a value of $Tu \sim 0.15\%$ in the vicinity of the leading edge. This value is obtained resolving the turbulence equations as described in Sec.(6.1).

6.2.2. Computational Domain

The grids were provided by Rui Lopes, from IST Lisbon. A set of 5 multiblock structured grids was generated with the GridPro software, with an O-topology encircling the spheroid. The computational domain is a box of total length $200L$ and width $100L$, where L is the length of the 6:1 prolate spheroid. The geometrical

center of the body is positioned at $x/L = 0$ and its distance from the boundaries is approximately $100L$. The incidence angles are imposed by rotating the spheroid with respect to its center, as well as an inner O-block around it. Thus, the flow is aligned with the x-axis. The grids are for half of the geometry, making use of a symmetry plane. The finest grid has 760 cells in the longitudinal direction, N_x, measured along the upper side of the surface, and 176 cells in the transversal direction, N_ϕ, measured along the plane located at half of the longitudinal length of the surface. The size of the first near wall cell in the direction normal to the surface is $\Delta y \sim 2.3 \times 10^{-6}$.

The finest grid counts 126016 cells on the surface of the spheroid, and a total of 42.5M volume cells. The remaining four grids are obtained from the finest one using the coarsening factors of 0.875, 0.75, 0.625 and 0.5. Mesh details are given in Table(1), where h_i is the typical cell size. It is defined as:

$$h_i = \frac{\sum_i^{N_{cell}} \Delta V_i}{N_{cell}}, \tag{86}$$

where ΔV_i is the volume of the i-th cell, and N_{cell} is the total number of cells. The coarsest grid from different points of view is shown in Fig.(6) and (7).

	N_{cells}	$N_{surface}$	h_i/h_1	$y^+_{\max}$
Grid1	42.6M	126016	1	0.4
Grid2	28.3M	95816	1.14	0.46
Grid3	17.9M	70884	1.33	0.54
Grid4	10.3M	48750	1.61	0.65
Grid5	5.3M	31504	2	0.8

Table 1: 6:1 Prolate Spheroid: Mesh details.

The inlet conditions for the angles of attack under study are reported in Table(2): the turbulence intensity Tu_{in} and the eddy viscosity ratio $(\nu_t/\nu)_{in}$ at the inlet, and the value of turbulence intensity Tu predicted in the vicinity of the body .

Geometry	α	Re	$Tu_{in}(\%)$	$(\nu_t/\nu)_{in}$	$Tu(\%)$
6:1 Prolate Spheroid	5° 15° 30°	6.5×10^6	0.5	250	0.15

Table 2: 6:1 Prolate Spheroid: Computations details.

6.2.3. Computational Costs

All the computations around the 6:1 prolate spheroid were run on national HPC resources. For each grid, the interpolated solution from its correspondent "one level coarser" grid is used as initial solution. The computations by $\gamma + CF$ on the coarsest grid, Grid5, were run on 280 processors, for $\sim$ 9000 CPU hours of simulation to converge. Convergence is controlled by a gain of minimum four orders of the normalized residuals for all the turbulence and transition variables and by forces convergence. It is worthwhile to mention that the convergence of the non-linear residuals in L_2 norm is very noisy, because of the presence of several min, max limiters in the original γ formulation, which are not smooth functions. This problem has already been observed also for 2D simulations, Lopes, [3]. Simulations on finer meshes were run on an higher number of processors, up to a maximum of 784.

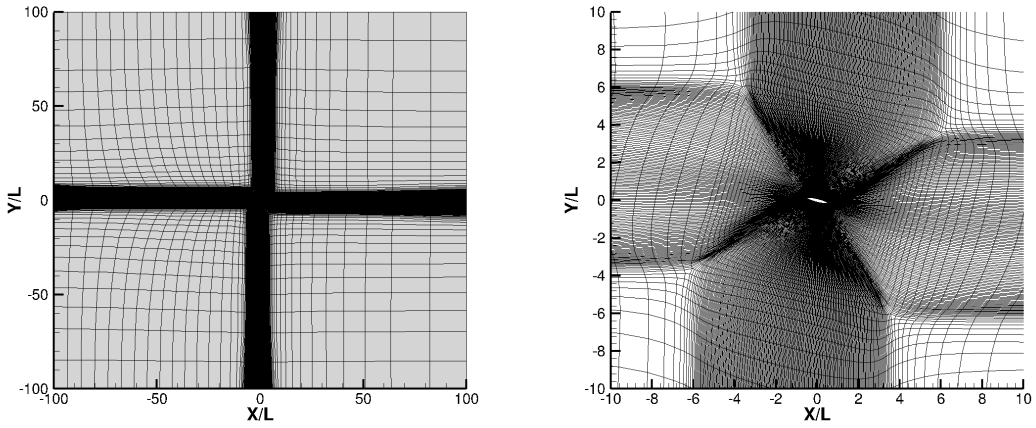

(a) Full Computational Domain.

(b) Zoom on the O-block surrounding the spheroid.

Figure 6: 6:1 prolate spheroid: $\alpha = 15°$. Full domain and close up on the O-block surrounding the body for the coarsest mesh.

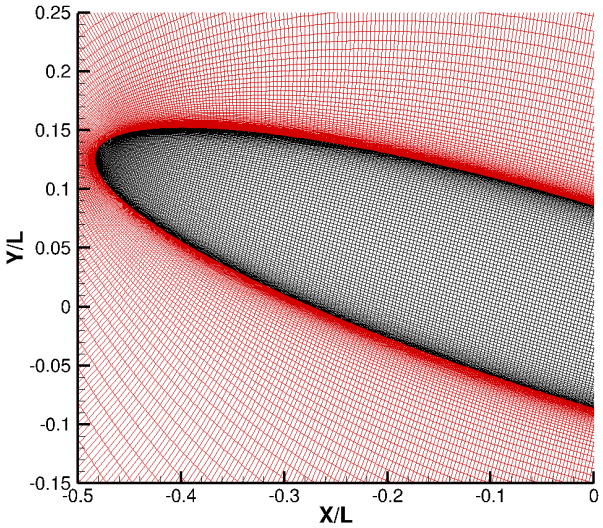

(a) Surface mesh (black), mesh on the symmetry plane (red).

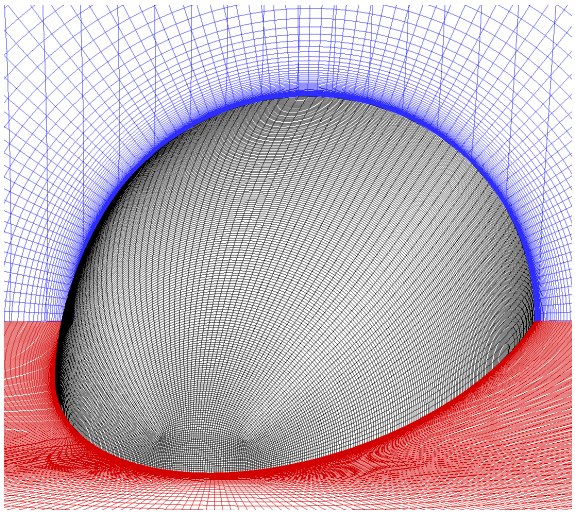

(b) Surface mesh (black), mesh on the symmetry plane (red), mesh on the plane $X/L = 0$ (blue).

Figure 7: 6:1 prolate spheroid. Coarsest mesh at $\alpha = 15°$, closed up on the first half of the spheroid: surface mesh, mesh on the symmetry plane, mesh in the wall normal direction on the plane $X/L = 0$.

6.2.4. Results: $\alpha = 15°$

Results by $\gamma + CF$ model for the angle of attack $\alpha = 15°$ were computed on all the five provided grids. Convergence results of friction and pressure drag coefficient with respect to the grid refinement are shown in Fig.(8). The estimation of the convergence order p of the discretization method relies on Richardson

Extrapolation (RE), following the procedure from Eça *et al.*, [28], [29], [30]. Relying on RE, the exact solution ϕ_0 can be expanded in respect of the discrete solution ϕ_i as

$$\phi_0 = \phi_i(x) + h_i^p \alpha + o(x, h_i^q). \tag{87}$$

$o(x, h_i^q)$ includes all the terms of order $q > p$. The index i relates to the different grids on which the solution ϕ_i is computed and α is the error constant. The parameter h_i is the typical cell size, as defined in Eq.(86). Based on the expansion in Eq.(87), the discretization error δ_{RE} can be written as

$$\delta_{RE} = \phi_i - \phi_0 = \alpha h_i^p. \tag{88}$$

This expansion can be manipulated to obtain an expression for the order of convergence p. It is observed that an estimated order of convergence $p = 2$ of the discretization error is obtained on the friction component, as theoretically expected for a finite volume method. The pressure drag presents a quasi-2nd order convergence with respect to the grid refinement. The behavior of the pressure is not worrying, but related to the noisy convergence of the non-linear residuals. It is also noticed that $C_{d,f}$ decreases with the grid refinement. γ transition model works first installing turbulence in the boundary layer and further destroying it throughout the simulation. The intermittency is overestimated on coarser grids, resulting in a slightly wider turbulent region. In terms of drag coefficients, the results on the three finest grids are very similar. The same observation is valid for the skin friction C_f contours and transition onset predictions. Results for $\alpha = 15°$ are shown on Grid1 of Table(1).

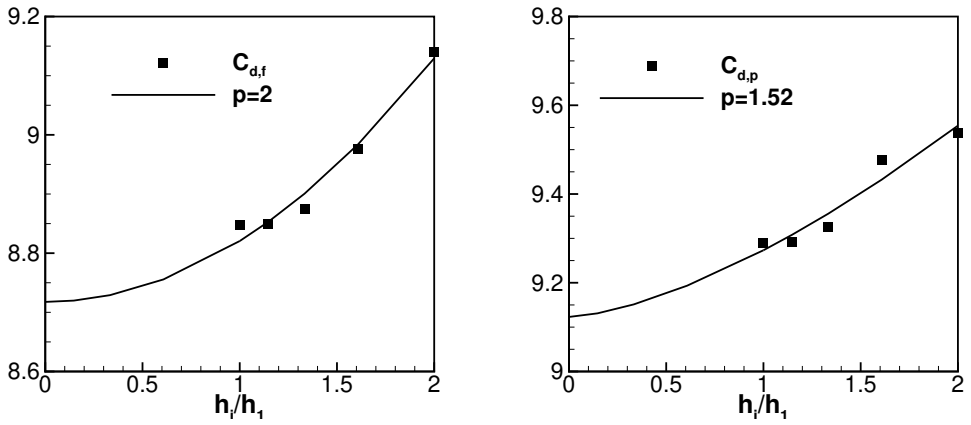

(a) $C_{d,f}$. (b) $C_{d,p}$.

Figure 8: 6:1 Prolate Spheroid: $\alpha = 15°$. Convergence of pressure and viscous drag for $\gamma + CF$ formulation with respect to the grid refinement. p is the estimated convergence order of the discretization error relying on Richardson Extrapolation.

The experimental C_f contours are presented in Fig.(9a) in the $X/L - \phi$ plane, where the variable ϕ is the azimuthal angle. $\phi = 0°$ corresponds to the windward symmetry plane, $\phi = 180°$ to the leeward one.

For this angle of attack and Reynolds number, a zone of CF-dominated transition is observed in correspondence of the middle of prolate spheroid. The kink, at about 20% of the length of the spheroid and $\phi \sim 130°$, marks the change of the transition process. The transition process on the leeward side is driven by T-S waves. The numerical skin friction contours computed by $\gamma + CF$ are presented in Fig.(9d). They are also compared to the predictions by γ without crossflow inclusion, Fig.(9b), referred to as γ, and γ coupled to the $Tc1$ crossflow criterion, as published by Menter & Smirnov, Fig.(9c). For the latter, here denominated $\gamma + Tc1$-MS, no information was given in the original publication of Menter & Smirnov about the criterion inclusion in γ formulation, except from their definition of the $Tc1$, here referred to as $Tc1_{MS}$. Their crossflow criterion is defined as:

$$Tc1_{MS} = \frac{G_{MS}\Psi Re_V}{150}. \tag{89}$$

In Eq.(89), G_{MS} formulation is given by

$$\begin{aligned} g(\lambda_{CF-MS}) &= 8.8\lambda^3_{CF-MS} - 9.1\lambda^2_{CF-MS} + 3.7\lambda_{CF-MS} + 1 \\ g(\lambda_{CF-MS}) &= \min[\max(g(\lambda_{CF-MS}), 1), 2.3] \\ G_{MS}(\lambda_{CF-MS}) &= \frac{0.684}{g(\lambda_{CF-MS})}, \end{aligned} \tag{90}$$

where λ_{CF-MS} is:

$$\lambda^*_{CF-MS} = -0.1111 \cdot \frac{d\mathrm{v}}{dy}\frac{y^2}{\nu} + 2.3, \tag{91}$$

$$\lambda_{CF-MS} = \min[\max(\lambda^*_{CF-MS}, 0), 0.7]. \tag{92}$$

In the presented simulations, it was decided for the following formulation for the $F_{onset,CF-MS}$ in $\gamma + Tc1 - MS$ model:

$$F_{\mathrm{onset1},CF-MS} = Tc1_{MS}/c \tag{93}$$

$$F_{\mathrm{onset2},CF-MS} = \min[\max(F_{\mathrm{onset1},CF-MS}, 0), 2], \tag{94}$$

$$F_{\mathrm{onset3},CF-MS} = \max(1 - (R_T/a)^3, 0), \tag{95}$$

$$F_{\mathrm{onset},CF-MS} = \max(F_{\mathrm{onset2},CF-MS} - F_{\mathrm{onset3},CF-MS}, 0), \tag{96}$$

$$a = 1.5, c = 0.6. \tag{97}$$

The final F_{onset} that enters the intermittency production term is the same as in Eq.(9), where $F_{\mathrm{onset},CF-MS}$ substitutes $F_{\mathrm{onset},CF}$. In conclusion,the differences between $\gamma + CF$ and $\gamma + Tc1$-MS variants lie in the definition of the function pressure function, G vs G_{MS}, as well as the pressure gradient parameter approximation, λ_{CF} vs λ_{CF-MS}, because of the introduction of the sweep angle ϕ.

In general, it is clearly visible that a correlation that accounts for crossflow instabilities is fundamental. The skin friction contours as computed with and without crossflow criterion considerably differ. A zone of pure crossflow transition is observed at the middle of the spheroid down to the windward side. CF instabilities also contribute to transition close to the leeward symmetry plane. The predictions by $\gamma + CF$ are in very good agreement with the measurements within the range $30° < \phi < 120°$. Discrepancies are observed close to the two symmetry planes. The proposed calibration considerably enhances the performance of the $Tc1$ criterion, see Fig.(9c) vs Fig.(9d), predicting a considerable fuller transition front. By including the sweep angle, it is accounted for its impact on the overall transition process. Compared to a swept wing, the 6:1 prolate spheroid, is a geometry significantly more swept. If the region next to the stagnation point is excluded, the windward symmetry plane looks like the attachment line of a cylinder with a geometrical sweep angle $\Phi = \frac{\pi}{2} - \alpha$, with α angle of attack, as discussed by Arnal, in [31]. For the specific case of $\alpha = 15°$, the geometrical sweep angle at the symmetry plane would be $\Phi \sim 75°$ and it could be expected a local sweep angle ϕ of this order on the windward side.

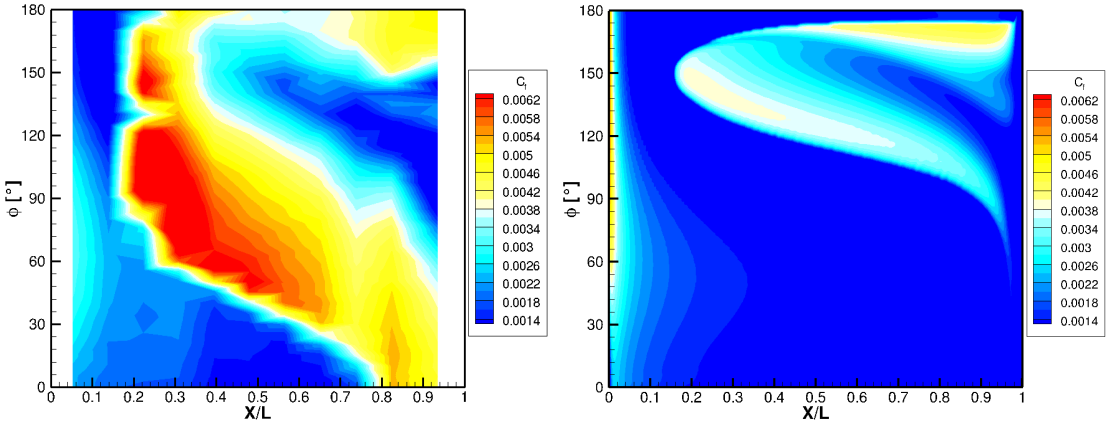

(a) $X/L - \phi$ plane. Measured C_f distribution.

(b) $X/L - \phi$ plane. Predicted C_f distribution by γ.

(c) $X/L - \phi$ plane. Predicted C_f distribution by $\gamma + Tc1$-MS.

(d) $X/L - \phi$ plane. Predicted C_f distribution by $\gamma + CF$.

Figure 9: 6:1 Prolate Spheroid: $\alpha = 15°$. Measured and predicted skin friction C_f distributions. Numerical results are computed using γ and $\gamma + CF$ models . The results obtained with $\gamma + Tc1$-MS, with the $Tc1$ version of Menter & Smirnov, are also shown.

Fig.(10) to Fig.(12) present the girthwise skin friction distribution at different sections. Results from Menter & Smirnov Tc1 version, $\gamma + Tc1$-MS, are not considered in these plots. At $X/L = 0.223$, it is visible that $\gamma + CF$ predicts an uniform and fuller transition front with respect to the experiments, without any visible kink. For $\phi < 120°$, $\gamma + CF$ is able to predict the transition that γ completely neglects. The different estimation of C_f close to the leeward side ($\phi > 130°$) by $\gamma + CF$ and γ, from $X/L = 0.223$ on, is related to the fact that $\gamma + CF$ promotes transition upstream compared to γ, as effect of the crossflow inclusion. This behavior is due to the fact that C1-based criteria have the tendency to predict transition upstream

when associated with T-S criteria, Bégou, [32]. In general, using $\gamma + CF$ the intermittency production term activates more upstream than using γ, as well as the destruction of intermittency, E_γ. Thus, at each section chosen for the comparison, it results that E_γ, which is proportional to $\gamma(1-\gamma)$, is stronger in the computations by $\gamma + CF$ than the ones from γ, explaining the lower C_f.

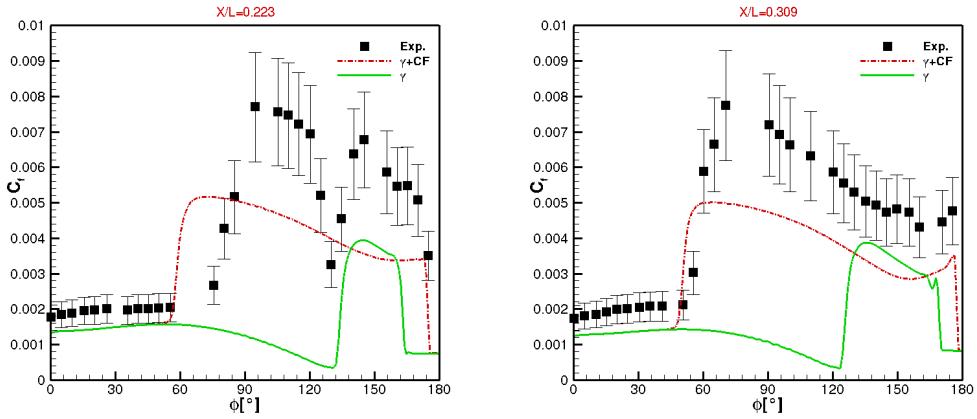

(a) $X/L = 0.223$. (b) $X/L = 0.309$.

Figure 10: 6:1 Prolate Spheroid: $\alpha = 15°$. Experimental and numerical girthwise distribution of C_f at the sections $X/L = 0.223$ and $X/L = 0.309$. Numerical results are computed with $\gamma + CF$ and γ models. At each validation point, the experimental uncertainty is reported.

In the skin friction contours computed by $\gamma + CF$, shown in Fig.(9d), it can be observed a tongue of delayed transition close to the symmetry plane. The laminar tongue appears at section $X/L = 0.223$ and it is visible until section $X/L = 0.395$, see Fig.(10a) and Fig.(11a). This is a mesh effect, rather than an erroneous prediction. Indeed, some crossflow occurs close to the vertical symmetry plane, as also suggested by γ predictions. Nevertheless, because of the symmetry plane, the streamlines are forced to follow the gridlines, delaying the transition process. This laminar tongue is grid dependent and its extent is reduced on coarser grids. Over all, the C_f predictions by $\gamma + CF$ are underestimated with respect to the experiments, but this quantitative discrepancy lies within the range of the experimental uncertainties. This under-estimation is related to the unknown free-stream turbulence level used in the experiments. Different values of Tu, within the range $0.1\% - 0.3\%$, affect the C_f quantitatively. The Tu used in the simulations is most probably lower than what found experimentally.

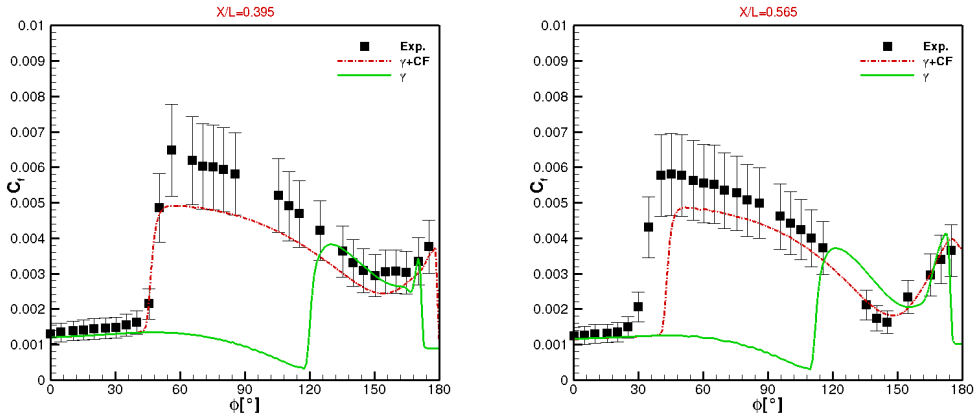

(a) $X/L = 0.395$. (b) $X/L = 0.565$.

Figure 11: 6:1 Prolate Spheroid: $\alpha = 15°$. Experimental and numerical girthwise distribution of C_f at the sections $X/L = 0.395$ and $X/L = 0.565$. Numerical results are computed with $\gamma + CF$ and γ models. At each validation point, the experimental uncertainty is reported.

Approaching the trailing edge of the body, $\gamma + CF$ model does not predict transition for $\phi < 30°$ and the flow close to the windward symmetry plane remains laminar until the last section. Measurements and predictions start deviating from the section $X/L = 0.565$, see Fig.(11b) up to the trailing edge $X/L = 0.936$, see Fig.(12b).

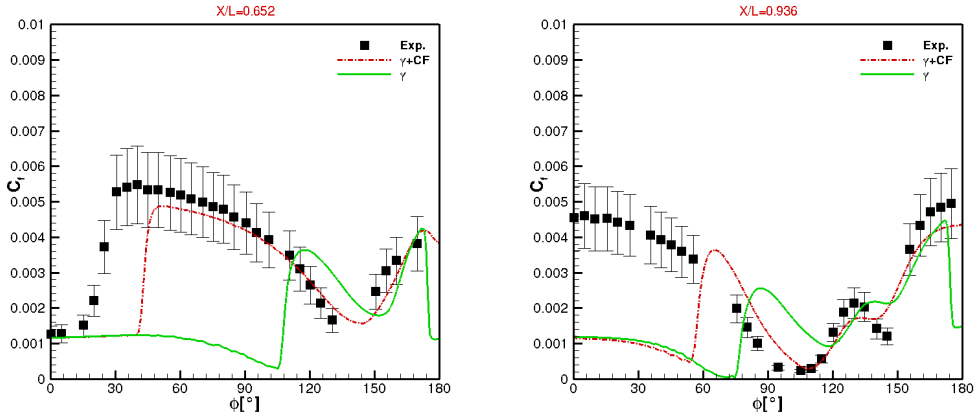

(a) $X/L = 0.652$. (b) $X/L = 0.936$.

Figure 12: 6:1 Prolate Spheroid: $\alpha = 15°$. Experimental and numerical girthwise distribution of C_f at the sections $X/L = 0.652$ and $X/L = 0.936$. Numerical results are computed with $\gamma + CF$ and γ models. At each validation point, the experimental uncertainty is reported.

Close to the symmetry plane, transition is hardly due to pure crossflow. Actually, at the symmetry plane,

no crossflow transition can happen, because the crossflow component of the velocity is zero. This incorrect flow prediction at the windward side is due to the fact that $\gamma + CF$ does not account for any transition mechanisms other than T-S waves and CF instabilities separately. Possible missing mechanisms are the non-linear interaction between T-S waves and crossflow instabilities, attachment line instabilities, and traveling crossflow modes. On the 6:1 prolate spheroid, for this angle of attack, some interaction between T-S and CF is expected. Nevertheless, the sum of the two $F_{\texttt{onset},*}$ functions, as given in Eq.(75), is probably not enough to account for the two modes interactions.

Leading edge instabilities are related to 2D boundary layer developing at the attachment-line. They can cause the flow to become turbulent along the longitudinal direction. This is a typical case where transition is dominated by streamwise instabilities, but the streamwise criterion Re_θ-based cannot predict it. As explained by Arnal, [31], for complex 3D flows where the streamlines are far from parallel, there is no implicit relation between Re_θ and the physical distance along which the instabilities propagates. For this reason, criteria which involve boundary layer parameters fail to predict transition at the attachment lines.

Traveling crossflow waves prevail over stationary modes for a turbulence level $Tu > 0.2\%$ and on smooth surfaces, as shown in the classic experiments by Deyhle & Bippes, [33]. The level of turbulence intensity reported in the experimental report by Kreplin is in a range for which traveling modes might be important and can occur around the prolate spheroid. The $Tc1$ criterion is based on Arnal's C1 criterion, which was empirically established based on experiences at very low free-stream turbulence levels, and it is not expected to predict traveling modes.

Skin friction lines predicted by $\gamma + CF$ are shown in Fig.(13). The model predicts an envelope of converging wall streamlines on the top of the spheroid coming from the windward and leeward sides, which are representative of an open-separation, according to the definition of Surana, [34].

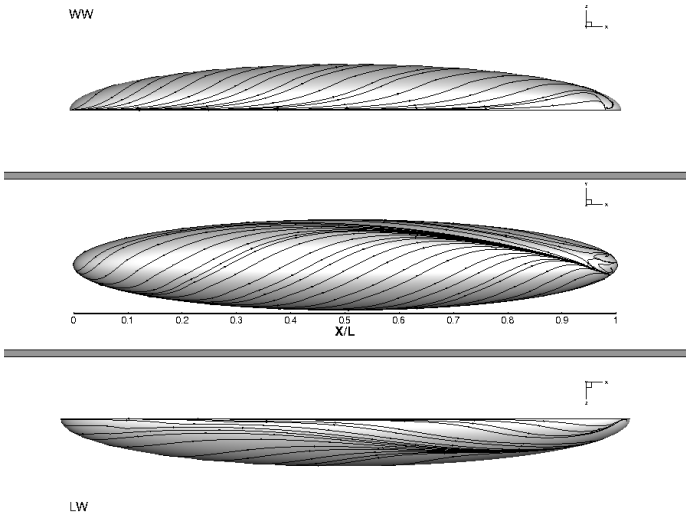

Figure 13: 6:1 Prolate Spheroid: $\alpha = 15°$. Skin friction lines as computed by $\gamma+CF$ model seen from different points of view, leeward (LW), top and windward (WW) sides.

The following sections are devoted to the analysis of the flow around the 6:1 prolate spheroid for $\alpha = 5°, 30°$. The presented computations are computed on Grid3 of Table(1). Indeed, considering the predicted transition front, computations on this grid are sufficiently accurate. Hereafter, the results computed with the original criterion by Menter & Smirnov, $\gamma + Tc1 - MS$, are not considered in the comparison.

6.2.5. Results: $\alpha = 5°$

The 6:1 prolate spheroid at $\alpha = 5°$ undergoes a different transition process than $\alpha = 15°$, nevertheless, the conclusions on the $\gamma + CF$ transition model performance are very similar. For the lowest angle of attack, the zone of pure crossflow transition is considerably reduced and concentrated in the middle of the spheroid. Transition on the windward side most probably occurs because of the non-linear interaction between T-S and CF instabilities. The experimental C_f contours in the $x/L-\phi$ plane are shown in Fig.(14a). Predictions by $\gamma + CF$ are shown in Fig.(14c). The inclusion of a crossflow criterion contributes to move upward the transition front in the region included in the range $70° < \phi < 160°$, if compared to γ results, shown Fig.(14b). Transition on the windward side is not predicted and this feature is related to the missing transition mechanism(s) that the model does not account for.

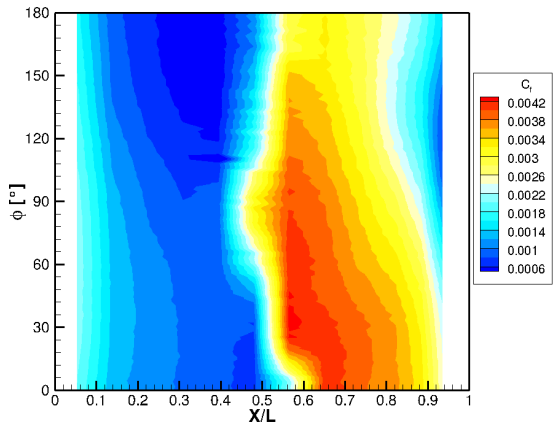

(a) $X/L - \phi$ plane. Measured C_f distribution.

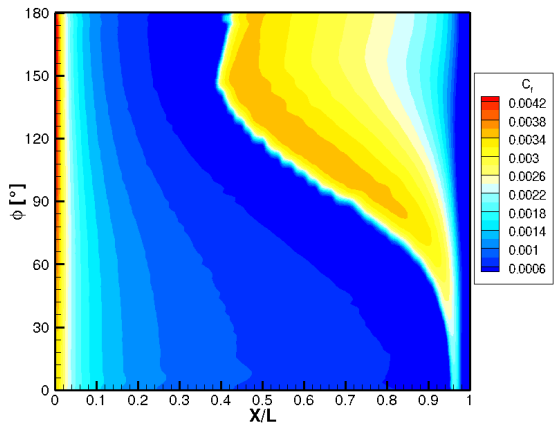

(b) $X/L - \phi$ plane. C_f distribution by γ .

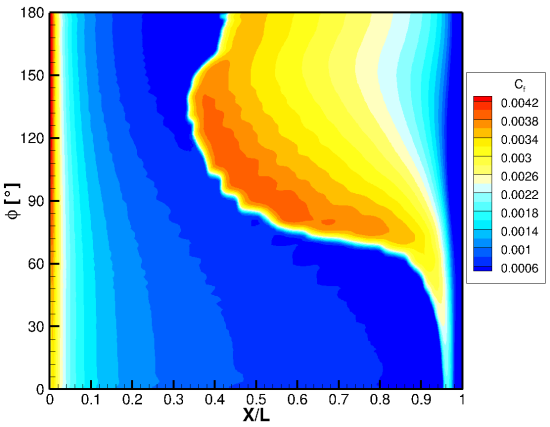

(c) $X/L - \phi$ plane: predicted C_f distribution by $\gamma + CF$.

Figure 14: 6:1 Prolate Spheroid: $\alpha = 5°$. Measured and predicted skin friction C_f distributions. Numerical results are computed using $\gamma + CF$ and γ models.

Fig.(15) to Fig.(16) show the girthwise distribution of the skin friction coefficient at different X/L planes, for $X/L \geqslant 0.480$. Only the second-half of the prolate spheroid is considered, because the flow is laminar in the first-half, as observed by the contours shown in Fig.(14). At section $X/L = 0.480$, Fig.(15a), transition close to the leeward symmetry plane, $\phi > 120°$, is due to the streamwise instabilities. At this location, simulations by both γ and $\gamma + CF$ predict the flow transition upward than in the experiments. Indeed, at $X/L = 0.480$, the measured skin friction girthwise profile suggests that the flow is still laminar close to the leeward symmetry plane.

Crossflow modes contribute to the transition predictions on the windward side. In general, $\gamma + CF$ predicts a transition profile fuller towards the windward side, down to $\phi \sim 60°$, compared to γ results, see Fig.(15). Nevertheless, the deviation between measurements and predictions by $\gamma + CF$ on the windward side is still considerable at all the analyzed sections. This is due to the fact that the interaction between T-S and CF mode is not accounted for by $\gamma + CF$ variant. Predictions by $\gamma + CF$ and γ become very similar towards the trailing edge, Fig.(16), close to the location where the flow is forced by the geometry to detach. Indeed, the skin friction lines as computed by $\gamma + CF$, shown in Fig.(17), do not show any characteristic topological sign of crossflow separation prior to the end of the body.

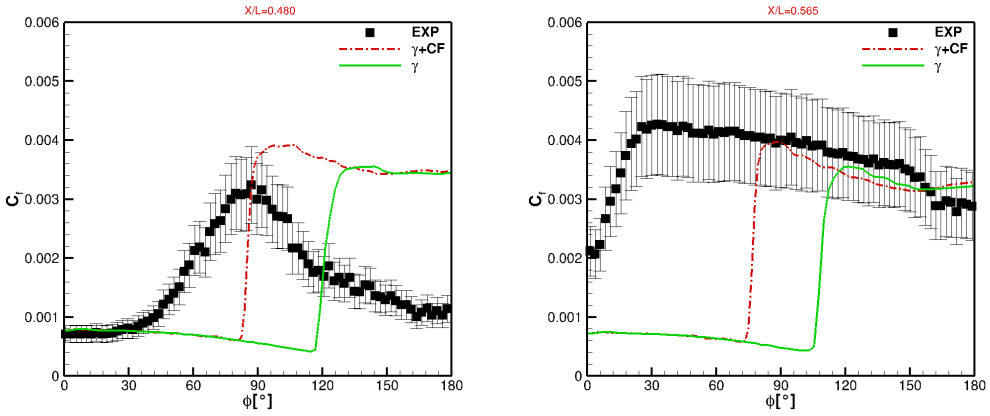

(a) $X/L = 0.480$. (b) $X/L = 0.565$.

Figure 15: 6:1 Prolate Spheroid: $\alpha = 5°$. Experimental and numerical girthwise distribution of C_f at the sections $X/L = 0.480$ and $X/L = 0.565$. Numerical results are computed with $\gamma + CF$ and γ models. At each validation point, the experimental uncertainty is reported.

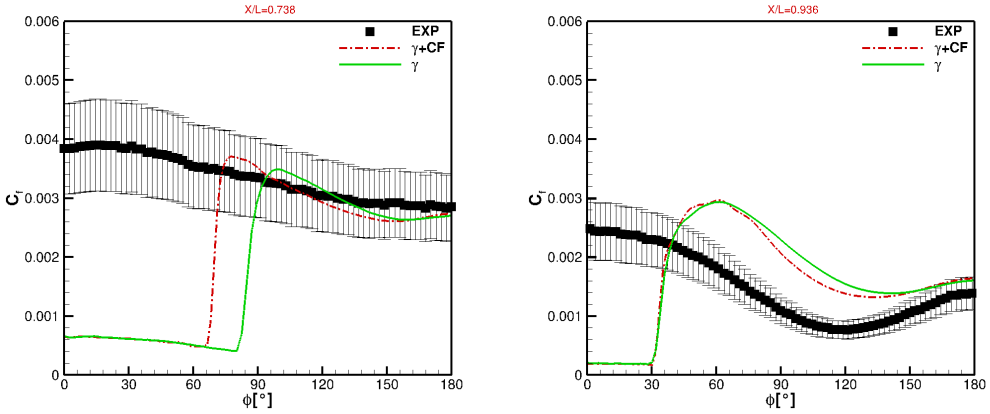

(a) $X/L = 0.738$. (b) $X/L = 0.936$.

Figure 16: 6:1 Prolate Spheroid: $\alpha = 5°$. Experimental and numerical girthwise distribution of C_f at the sections $X/L = 0.738$ and $X/L = 0.936$. Numerical results are computed with $\gamma + CF$ and γ models. At each validation point, the experimental uncertainty is reported.

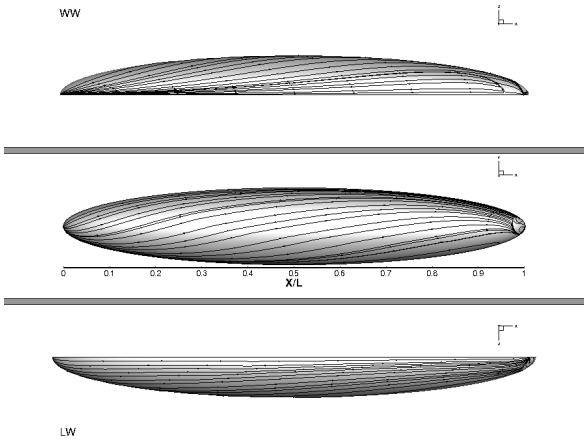

Figure 17: 6:1 Prolate Spheroid: $\alpha = 5°$. Skin friction lines as computed by $\gamma + CF$ model seen from different points of view, leeward (LW), top and windward (WW) sides.

6.2.6. *Results:* $\alpha = 30°$

The 6:1 prolate spheroid series is concluded with the angle of incidence $\alpha = 30°$, for which crossflow instabilities dominate the flow transition on a larger portion of the prolate spheroid, compared to the previous cases. No results for γ without crossflow are shown in this section. The experimental C_f contours are shown in Fig.(18a). Taking as a reference the section of the 6:1 prolate spheroid of maximum width, $X/L = 0.5$, the flow starts transitioning on the windward side at $\phi \sim 50°$ and transition completes at $\phi \sim 70°$. On the leeward side, the situation appears slightly more complicated. A laminar separation bubble occurs near

the nose of the spheroid: the flow separates and then rapidly reattaches. This separation-induced transition promotes the appearance of T-S waves on the leeward side of the spheroid that cause the flow to transition further downstream. The large skin friction values on the leeward side result from the induced velocities due to the separated vortex flow coming from the windward side, as mentioned in Kreplin.

The numerical C_f predictions by $\gamma + CF$ are shown in Fig.(18b). The new crossflow criterion performs very well on the windward side and transition predictions are in good agreement with experiments. In spite of the lower skin friction contours predicted by the transition model, the quantitative deviation between measured and predicted C_f is justified by the experimental uncertainties, as shown in Fig.(19).

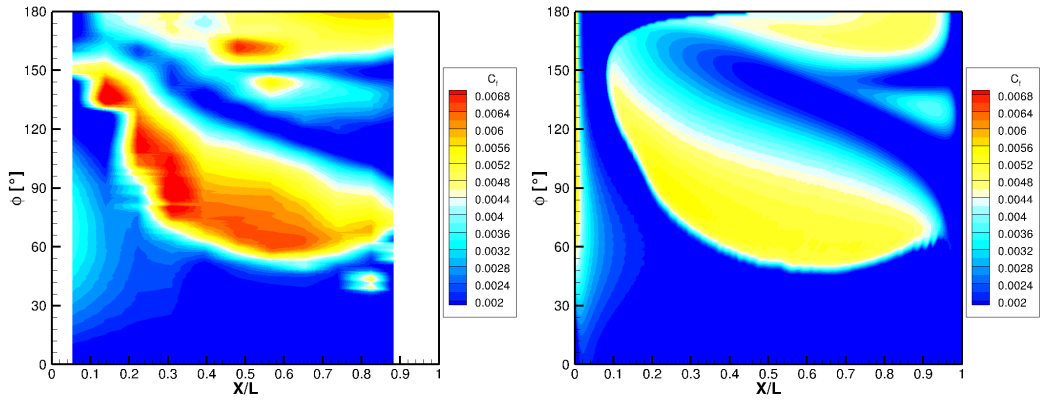

(a) $X/L - \phi$ plane: Measured C_f distribution.

(b) $X/L - \phi$ plane. Predicted C_f distribution.

Figure 18: 6:1 Prolate Spheroid: $\alpha = 30°$. Measured and predicted skin friction C_f distribution on the 6:1 prolate spheroid. Numerical results are computed using $\gamma + CF$ model.

Despite the good performance at the windward side, $\gamma + CF$ model fails to predict the correct transition features on the leeward side. The measured laminar separation bubble, right after the nose of the spheroid, is not reproduced in the simulations. The positive peak of C_f at $\phi \sim 150°$ in Fig(19a) and (19b) roughly indicates the transition location within the bubble. This is not visible in $\gamma + CF$ results. This discrepancy is related to γ model original formulation. The criterion that accounts for separation-induced transition is the additional production term in Eq.(28). Re_V in the first 20% of the spheroid length does not exceed the limiting value of 2200 to activate the additional production term of turbulence kinetic energy, Eq.(29). This behavior might be related to the diverging streamlines predicted at the leeward symmetry plane, close to the leading edge, Fig.(20), that cause the failure of the streamwise criterion, i.e. the differences between the physical distance along which the waves propagate and the distance along which the characteristic boundary layer thickness grows. The unpredicted laminar separation bubble pollutes further downstream

the numerical solution. The flow at the leeward side numerically transitions around $X/L = 0.139$, but the skin friction is systematically underestimated with respect to measurements, Fig.(19c) to Fig.(19f). Two different envelope of converging skin-friction lines are observed on the surface, one close to the middle of the spheroid, the other on the leeward side, as shown in Fig.(20). The separation line for the flow coming from the leeward side, which is the attracting portion of the skin friction line, can be roughly identified with respect to the minimum of the magnitude of the wall shear stress[1], according to Simpson, [35]. This second separation location occurs at the leeward side approximately around $X/L \sim 0.55$, but predicted skin friction lines are converging further downstream. The separation might be pushed downward because of the underpredicted laminar-to-turbulence transition within the boundary layer on the leeward side.

The local maximum peak of C_f at $X/L = 0.565$ at $\phi \sim 130°$, Fig.(19d), due to the velocity fluctuations induced by the separated vortex flow, is considerably pushed downward close to the trailing edge. Due to the large separation which the flow undergoes at such an high angle of attack, it cannot be excluded that the RANS turbulence model does not affect the overall results at separation. Indeed, they typically fail in massively separated region.

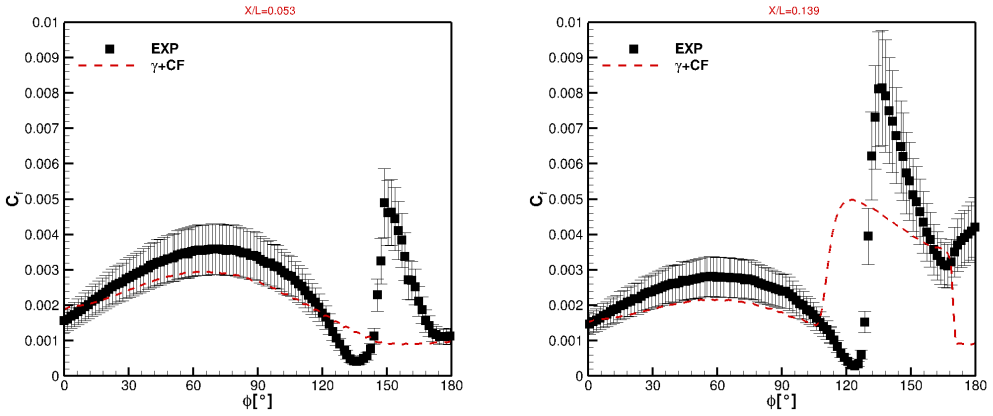

(a) $X/L = 0.053$. (b) $X/L = 0.139$.

[1]This is a fair approximation because the skin friction lines are converging from different sides of the prolate spheroid.

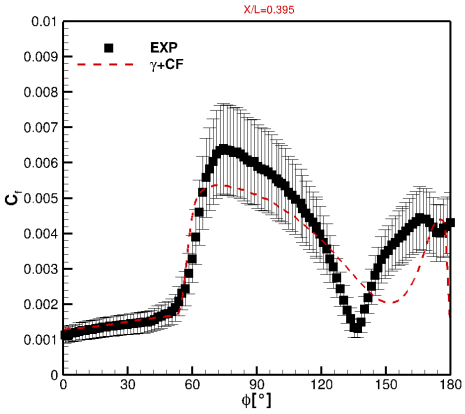

(c) $X/L = 0.395$.

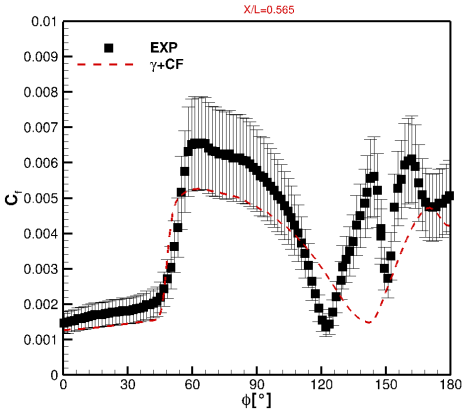

(d) $X/L = 0.565$.

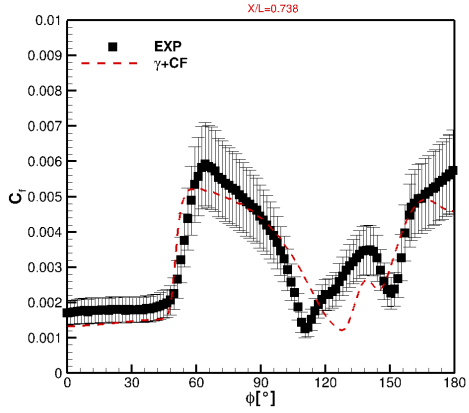

(e) $X/L = 0.738$.

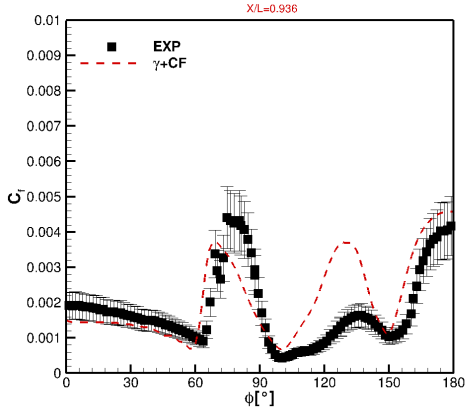

(f) $X/L = 0.936$.

Figure 19: 6:1 Prolate Spheroid: $\alpha = 30°$. Experimental and numerical girthwise distribution of C_f at different sections. Numerical results are computed with $\gamma + CF$ model. At each validation point, the experimental uncertainty is reported.

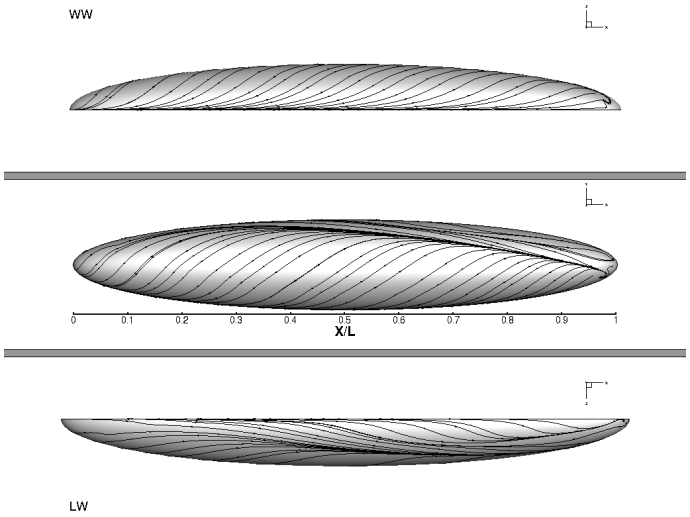

Figure 20: 6:1 Prolate Spheroid: $\alpha = 30°$. Skin friction lines as computed by $\gamma + CF$ model seen from different points of view, leeward (LW), top and windward (WW) sides.

6.3. Sickle Wing: CASE A

The last validation case is the sickle wing configuration. The wing design is conceived in order to generate a 3D boundary layer with increasing crossflow in the spanwise direction. Crossflow modes are highly amplified by the large spanwise gradients created in correspondence of the sweep kinks of the sickle shaped planform. The interest of the authors toward this geometry is to assess how much these strong spanwise gradients challenge the FSC assumptions, therefore the $Tc1$ crossflow criterion. Experimental data for different Reynolds numbers and angles of attack are available in Kruse *et al.*, [36]. The experimental campaign was run in an atmospheric, closed circuit type low-speed wind tunnel, the DNW-NWB in Braunschweig. The free-stream conditions are not given in Kruse's report. Nevertheless, it is mentioned that the average free-stream disturbance level is lower than in the experiments run from Petzold *et al.*, [37]. The latter were run around the same geometry, for the same Reynolds and incidence conditions, but in a different wind tunnel. Petzold *et al.* reported an average turbulence intensity of $Tu = 0.17\%$ that is used for the present computations.

6.3.1. Experimental Set Up

The wing consists of five sections: an unswept peniche raises the model above the tunnel wall, in order to avoid the contamination of the laminar boundary layer by the turbulent boundary layer at the tunnel wall. The central three swept sections, A, B, C are dedicated to transition measurements. Each segment has the same thickness and span length, but with increasing sweep $30°, 45°, 55°$, respectively. The wing is

completed by a tip, positioned at its outer extremity. Because of this particular design, the sickle wing experiences crossflow from the root towards its tip. The predominance of stationary crossflow instabilities over T-S waves in the transition process depends on the Reynolds number and angle of incidence. For the current simulations, the flow around the wing operating near its design point, at $Re = 2.75 \times 10^6$ and $\alpha = -2.6°$, is considered. For these conditions, T-S and CF waves occur at the same time. Each section presents a peculiar transition pattern. The transition location is detected by means of infrared thermography images and it is based on the increase of the convective heat flux due to turbulent mixing. Transition lines are extracted by infrared images using a temperature gradient detection scheme. The local transition position is recovered from the minimum on the temperature gradients, Kruse *et al.*, [38]. On the upper surface, transition on section A is dominated by T-S waves. Nevertheless, moving upstream in the spanwise direction, the transition process becomes to be CF-dominated. The zig-zag pattern, observed in the experiments, on section B and the first half of section C, indicates that transition is dominated by stationary crossflow. Transition on the lower surface occurs under a moderate adverse pressure gradient and it is T-S dominated. Experimental data included pressure tap measurements approximately along the midsection of each segment. The average model surface roughness of about 1.47 μm is neglected in the numerical simulations.

6.3.2. *Computational Domain*

The computational domain presented in Fig.(21) reproduces the wind tunnel dimension from the experiments of Kruse *et al.*. The inlet is located at $x/C = -4.6$ and the outlet at $x/C = 8.455$. The top and bottom walls are located at $z/C = \pm 1.633$ and the side wall at $y/C = 2.8$. In order to obtain the best agreement with the experimental results, the tunnel walls are treated as slip boundary conditions. No slip conditions are imposed on the body. The wing is turned with respect to the angle of incidence and the flow is aligned with x-axis. The mesh was generated using the hex-based unstructured grid generator HEXPRESS, and further refined using the systematic grid refinement (SGR) functionality implemented in the in-house flow solver ISIS-CFD. This SGR feature is a simplified variant of the adaptive grid refinement functionality: the grid is systematically refined without being controlled by any specific flow-feature. This approach allows to significantly improve the quality of the grid in the boundary layer and it is very useful when low-Re near wall grids need to be generated. Starting from an initial mesh of 10M of cells, with approximately 50 cells in the boundary layer, the mesh has been further refined with SGR in the longitudinal x-direction. In order to avoid an excessive refinement of the cells at the edges of the sickle wing, a maximum cell size equal to 1/4th of those in the x-direction has been imposed. The refinement procedure has been limited to the region next to the body, in order to avoid unnecessary cells in the free-stream. Different grid refinement levels have

been tested, nevertheless the one described above is relative to the grid used for the presented computations hereafter. The overall mesh is shown in Fig.(21a), as well as the mesh at the surface, Fig.(21b). In the latter figure, the solid red lines represent the boundaries between the three central swept sections, at which the geometrical sweep angle changes. Details on the mesh are shown in Table(3). The inlet conditions are reported in Table(4).

N_{cells}	$N_{surface}$	$y^+_{\max}$
54M	462243	0.436709

Table 3: Sickle Wing. Mesh details.

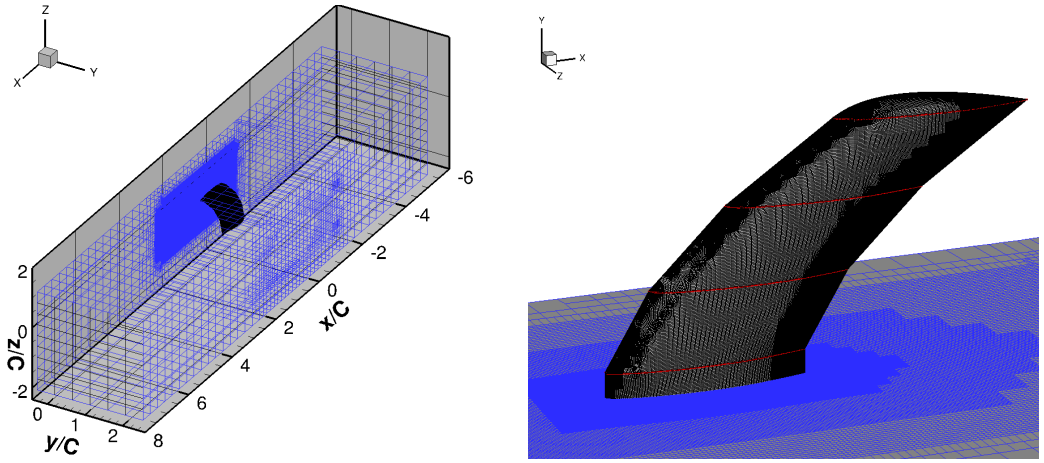

(a) Total computational domain.

(b) Mesh at the surface.

Figure 21: Sickle Wing. Grid used for the flow simulation around the sickle wing. Total computational domain and representation of the mesh at the surface. In Fig.(21b), the solid red lines represent the kink region, where the geometrical sweep angle changes.

α	Re	$Tu_{in}(\%)$	$(\nu_t/\nu)_{in}$	$Tu(\%)$
$-2.6°$	2.75×10^6	0.20	2.24	0.17

Table 4: Sickle Wing. Inlet conditions for the computations.

6.3.3. Computational Costs

The simulations for the sickle wing were run on HPC national resources as well. The simulation on the grid, whose details were given in Table(3), was performed on 784 processors for approximately $\sim$ 27440 CPU hours. The numerical solution by γ without crossflow inclusion has been used as initial solution for the computation by the crossflow variant of $\gamma + CF$.

6.3.4. Results

The skin friction contours on the upper and lower surface of the sickle wing are shown in Fig.(22). Predictions by γ without and with crossflow inclusion, γ and $\gamma + CF$ variants, respectively, are compared to the measurements. The latter consist of the extracted experimental transition lines on both surfaces. As a general remark, all the γ variants predict a jagged transition front. This is not due to the unsteadiness of the flow, but rather a consequence of the unstructured grid topology and the hanging nodes in the grid close to the boundary layer. The differences between predictions by γ and $\gamma + CF$ models are noticeable, especially on the upper surface, where transition is dominated by crossflow instabilities, Fig.(22a) vs Fig.(22c). γ predictions are in good agreement with measurements on Sec. A. Indeed, the transition model without crossflow inclusion is able to reproduce the laminar separation bubble that occurs towards the trailing edge. Moving upward, towards Sec. B, the measured transition line considerably changes in the spanwise direction, because of the amplification of stationary crossflow instabilities. As mentioned in Kruse *et al.*, [36], the sudden shift upward of the transition front in the middle of Section B is related to disturbances caused by the discrete roughness of the pressure tap row. The numerical simulation does not account for these roughness effects and $\gamma + CF$ predicts a more uniform transition front. On Section C, crossflow instabilities become weaker, as indicated by the downward shift on the transition front. This weakening is fairly represented in the numerical results by $\gamma + CF$ model. The turbulent wedges in the regions of sweep changeover are reasonably well predicted by $\gamma + CF$, despite the $Tc1$ calibration on FSC solutions, for which zero-spanwise gradients are assumed. They are nonetheless polluted by the discretization error committed at the junctions between the segments, where the spanwise gradients are considerably strong. In fact, the turbulent wedges predicted in the computations by $\gamma + CF$ model are diffused on their sides, and they are not as sharp as in the measurements. This discretization error is due to the fact that the grid at the surface is generally too coarse in the spanwise direction. Notably in correspondence of the junctions, i.e. the red lines at the surface in Fig.(21b), the mesh is not refined enough to predict accurately the strong spanwise gradients, that cause the turbulent wedges.

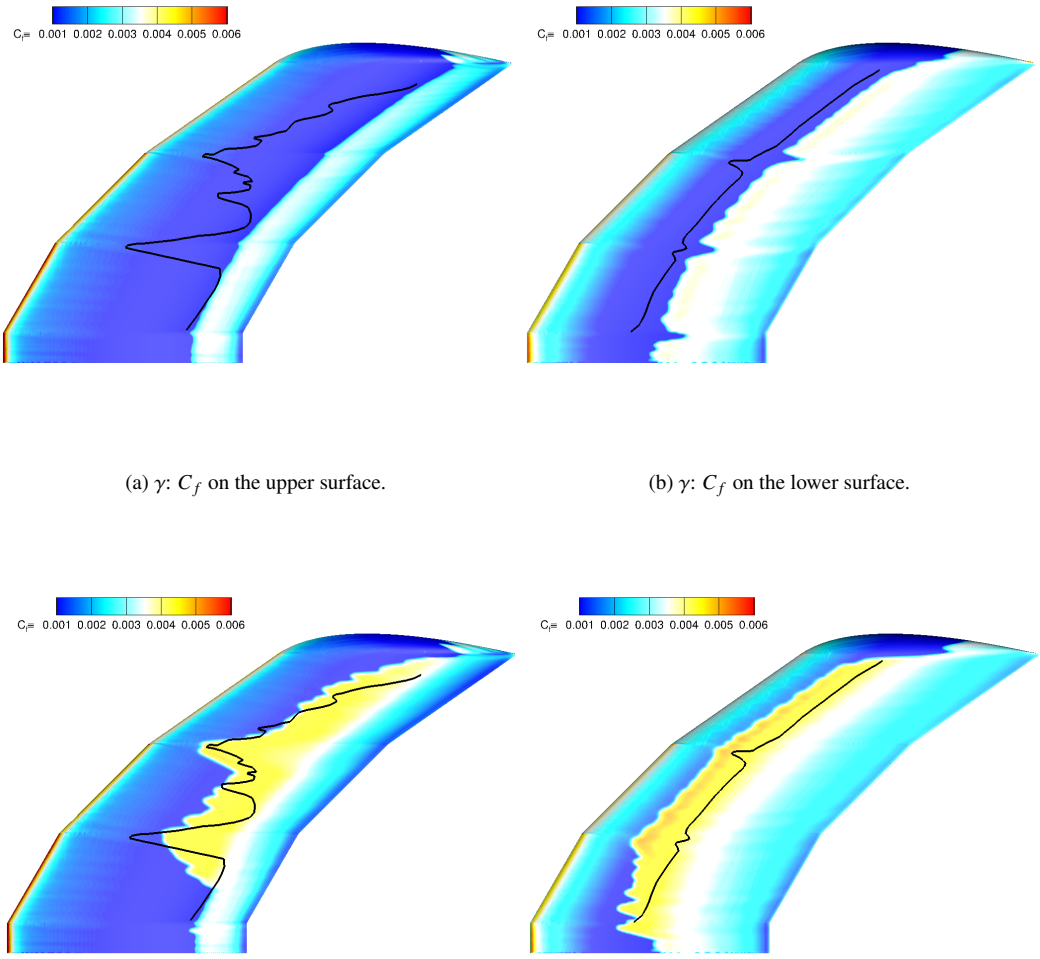

(a) γ: C_f on the upper surface.

(b) γ: C_f on the lower surface.

(c) $\gamma + CF$: C_f on the upper surface.

(d) $\gamma + CF$: C_f on the lower surface.

Figure 22: Sickle wing: $\alpha = -2.6°$. Predicted skin friction contours on the upper and lower surface of the sickle wing by γ and $\gamma + CF$ models. The black line is the extracted experimental transition location from Kruse *et al.*.

An accurate prediction of these wedges requires a very dense spanwise clustering of grid points across the boundaries of the three central segments composing the wing. These clusters of cells could be obtained by using HEXPRESS, since the spanwise direction is aligned with the axis z. Nevertheless, the thickness of the viscous sublayer would become very small and the overall quality of the grid in the boundary layer would not comply with what is needed for low-*Re* near wall transition models. Neither with the further use of SGR, it is possible to generate these spanwise cells clusters. Although the great potentiality of this approach, its main drawback is that it does not allow to control the surface aspect ratio of the grid at specific spanwise locations. Thus, the risk is that the overall number of cells might explode, reaching values that

are inconceivable for a RANS simulation. As example of a proper mesh that should be used for transition simulations around the sickle wing the reader should refer to Kim *et al.*, [39].

On the lower surface, the transition line is straight over the whole span. Transition is dominated by T-S waves. The crossflow criterion should contribute to the small kinks in the wing planform. Nevertheless, $\gamma + CF$ reproduces these features to a lesser extent, and the transition line is predicted upstream of the experimental front, Fig.(22d). This behavior is related to the discretization error that pollutes the overall results and an excessive diffusion of the intermittency γ. The measured and calculated pressure coefficient distributions are presented in Fig.(23), as extracted along each midsection. The numerical results are computed with γ and $\gamma + CF$ transition model. Over all, a very good agreement is achieved between numerical and experimental results at each analyzed section. The numerical C_p is underestimated by both γ variant at Sec.B, Fig.(23b), on the lower surface, i.e. the minimum computed C_p is lower than the measured one. Nevertheless, such quantitative differences are not relevant to transition predictions, that are affected by the pressure gradients. At all sections on the upper surface, the favorable pressure gradient region is considerably extended. On Sec.A, Fig.(23a), the pressure distribution indicates the presence of the small laminar separation bubble mentioned above. The laminar separation point is approximately located at $x/C \sim 0.75$. This flow feature is only predicted by γ model, without crossflow inclusion. The latter also predicts laminar separation bubbles approximately at the same position for all the other sections that are not observed in the experimental results. On the lower side, where transition is dominated by adverse pressure gradients, only γ, without CF, is able to reproduce the characteristic wiggles between $x/C \sim 0.35$ and $x/C \sim 0.40$. These flow features are not predicted by $\gamma + CF$, nevertheless their absence does not affect the overall transition process, if evaluated with respect to the C_f contours.

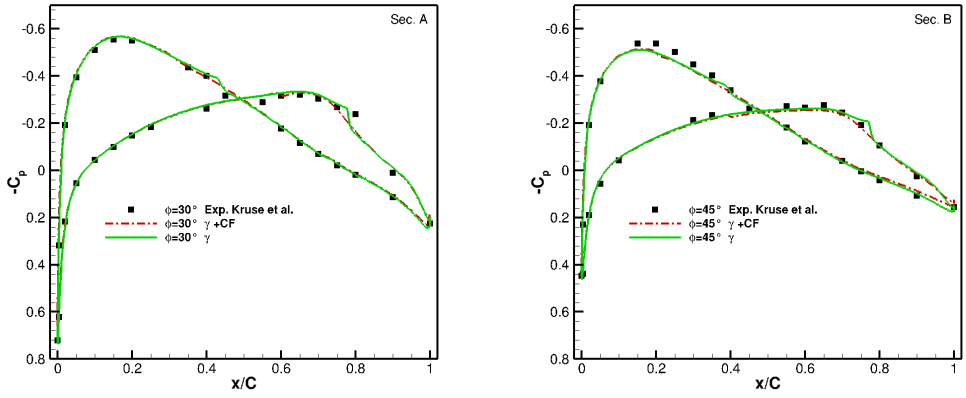

(a) Sec. A

(b) Sec. B

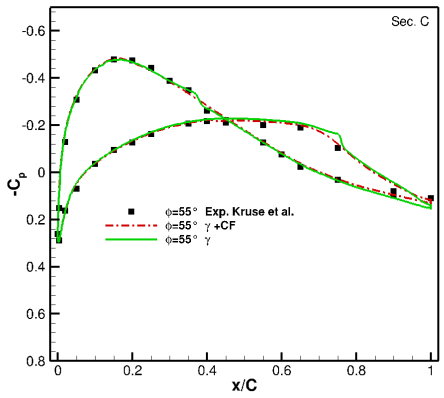

(c) Sec. C

Figure 23: Sickle wing: $\alpha = -2.6°$. Comparison of measured and calculated pressure coefficient distributions at each sweep section of the model, from Section A to Section C. Numerical results are computed by γ and $\gamma + CF$ models.

7. Conclusion

This work was devoted to the analysis of $\gamma + CF$ transition model performance for 3D boundary layers. The recalibrated $Tc1$ criterion here presented is used for the inclusion of transition due to stationary crossflow vortices. $\gamma + CF$ variant was proven to perform well on the two tested geometries, the 6:1 prolate spheroid and the sickle wing, at different angles of attack. Within the new re-calibrated $Tc1$, it is accounted for the variation of the pressure gradient parameter in the streamwise direction with respect to the local sweep angle and its influence on the overall crossflow transition process. This modification strongly enhances

the original $Tc1$, as published by Menter & Smirnov. $\gamma + CF$ performs very well around the 6:1 prolate spheroid at different angles of incidence. The unpredicted flow transition on the windward side is not crossflow related, but is due to missing physics within the mathematical model formulation. Possible physical mechanisms that $\gamma + CF$ does not account for are the non-linear interactions between crossflow and T-S waves, attachment line instabilities, and traveling crossflow. In spite of the $Tc1$ calibration with respect to the solutions of the Falkner-Skan-Cooke equations, which assume zero-spanwise gradients, the results for the flow around the sickle wing are very encouraging. $\gamma + CF$ model is able to predict the turbulent wedges at the junctions of the sickle shaped planform, due to the local amplification of stationary crossflow modes. However, the discretization error resulting from the coarseness of the mesh at the junctions between the three central swept section pollutes the result. Strategies to create a proper mesh within Hexpress are currently under study. Future works will be devoted to the inclusion of the non-linear interaction effects of crossflow and Tollmien-Schlichting modes within $\gamma + CF$ formulation. It is the authors belief that including additional correlations accounting for other transition mechanisms is crucial to further validate the modeling performance of RANS γ model.

8. ACKNOWLEDGMENTS

The computations were performed using HPC resources from GENCI (Grand Equipement National de Calcul Intensif) (Grant-A0102A00129), which is gratefully acknowledged. The help of Dr. Rui Lopes from IST Lisbon who provided us with the structured grids for the 6:1 prolate spheroid is warmly acknowledged. The help of Prof.Dr.Ing. Rolf Radespiel from TU Braunschweig, who provided us with these experimental data from the Sickle Wing, is kindly acknowledged. Finally, Prof. Christophe Airiau from Paul Sabatier University in Toulouse is sincerely acknowledged for sharing his Falkner-Skan-Cooke solver with the authors.

References

[1] F. Menter, R. Langtry, Transition modelling for turbomachinery flows, Low Reynolds Number Aerodynamics and Transition (2012) 31–58 (2012).

[2] F. Menter, P. Smirnov, T. Liu, R. Avancha, A one-equation local correlation-based transition model, Flow, Turbulence and Combustion 95 (4) (2015) 583–619 (2015).

[3] R. Lopes, Simulation of transition from laminar to turbulent regime in practical applications of incompressible flow, Ph.D. thesis, Universidade de Lisboa-Instituto Superior Técnico (2021).

[4] G. Rubino, Laminar-to-turbulence transition modeling of incompressible flows in a rans framework for 2d and 3d configurations, Ph.D. thesis, Ecole Centrale de Nantes (2021). arXiv:https://doi.org/10.2514/1.42362, doi:10.2514/1.42362.

[5] C. Müller, F. Herbst, Modelling of crossflow-induced transition based on local variables, no. 2252, 2014, p. 72 (2014).

[6] R. Langtry, Extending the γ-re_θ correlation based transition model for crossflow effects, in: 45th AIAA Fluid Dynamics Conference, 2015, p. 2474 (2015).

[7] C. Grabe, N. Shengyang, A. Krumbein, Transport modeling for the prediction of crossflow transition, AIAA Journal 56 (8) (2018) 3167–3178 (2018).

[8] V. Schmitt, F. Manie, Ecoulements subsoniques et transsoniques sur une aile en flèche variable, La Recherche Aérospatiale (1979) 219–237 (1979).

[9] ONERA, Research done at DERAT (october 1982 through september 1983); summary of principal results obtained (1984).

[10] J. Dagenhart, W. Saric, Crossflow stability and transition experiments in swept-wing flow (1999).

[11] H. Kreplin, H. Vollmers, H. Meier, Wall shear stress measurements on an inclined prolate spheroid in the DFVLR $3m \times 3m$ low speed wind tunnel, Data Report, DFVLR IB (1985) 222–84 (1985).

[12] F. Menter, P. Smirnov, Development of a RANS-based model for predicting crossflow transition, in: In Proceedings of the Contributions to the 19th STAB/DGLR Symposium, München, Germany, 2014 (2014).

[13] D. Arnal, M. Habiballah, E. Coustols, Théorie de l'instabilité laminaire et critères de transition en écoulement bi et tridimensionnel, La Recherche Aérospatiale (2) (1984) 125–143 (1984).

[14] D. Poll, Some aspects of the flow near a swept attachment line with particular reference to boundary layer transition (1978).

[15] F. W. Boltz, G. C. Kenyon, C. Q. Allen, Effects of sweep angle on the boundary-layer stability characteristics of an untapered wing at low speeds, National Aeronautics and Space Administration, 1960 (1960).

[16] J. C. Cooke, The boundary layer of a class of infinite yawed cylinders, Mathematical Proceedings of the Cambridge Philosophical Society 46 (4) (1950) 645–648 (1950).

[17] P. Queutey, M. Visonneau, An interface capturing method for free-surface hydrodynamic flows, Computers & Fluids 36 (9) (2007) 1481–1510 (2007).

[18] A. Leroyer, M. Visonneau, Numerical methods for ranse simulations of a self-propelled fish-like body, Journal of Fluids and Structures 20 (7) (2005) 975–991 (2005).

[19] J. Wackers, G. Deng, A. Leroyer, P. Queutey, M. Visonneau, Adaptive grid refinement for hydrodynamic flows, Computers & Fluids 55 (2012) 85–100 (2012).

[20] J. Wackers, G. Deng, E. Guilmineau, A. Leroyer, P. Queutey, M. Visonneau, A. Palmieri, A. Liverani, Can adaptive grid refinement produce grid-independent solutions for incompressible flows?, Journal of Computational Physics 344 (2017) 364–380 (2017).

[21] E. Guilmineau, O. Chikhaoui, G. Deng, M. Visonneau, Cross wind effects on a simplified car model by a DES approach, Computers & Fluids 78 (2013) 29–40 (2013).

[22] B. P. Leonard, A stable and accurate convective modelling procedure based on quadratic upstream interpolation, Computer Methods in Applied Mechanics and Engineering 19 (1) (1979) 59–98 (1979).

[23] F. Menter, M. Kuntz, R. Langtry, Ten years of industrial experience with the sst turbulence model, Turbulence, heat and mass transfer 4 (1) (2003) 625–632 (2003).

[24] M. Kato, B. Launder, The modelling of turbulent flow around stationary and vibrating square cylinders, in: The 9th Symposium of Turbulent Shear Flows, 1993, pp. 10–4 (1993).

[25] M. Högberg, D. Hennigson, Secondary instability of cross-flow vortices in Falkner–Skan–Cooke boundary layers, Journal of Fluid Mechanics 368 (1998) 339–357 (1998).

[26] J. H. Choi, O. J. Kwon, Recent improvement of a correlation-based transition model for simulating three-dimensional boundary layers, AIAA Journal 55 (6) (2017) 2103–2108 (2017).

[27] P. R. Spalart, C. L. Rumsey, Effective inflow conditions for turbulence models in aerodynamic calculations, AIAA Journal 45 (10) (2007) 2544–2553 (2007).

[28] L. Eça, M. Hoekstra, Evaluation of numerical error estimation based on grid refinement studies with the method of the manufactured solutions, Computers & Fluids 38 (8) (2009) 1580–1591 (2009).

[29] L. Eça, G. Vaz, M. Hoekstra, A verification and validation exercise for the flow over a backward facing step, in: Fifth European Conference on Computational Fluid Dynamics, 2010, pp. 14–17 (2010).

[30] L. Eça, M. Hoekstra, A procedure for the estimation of the numerical uncertainty of CFD calculations based on grid refinement studies, Journal of Computational Physics 262 (2014) 104–130 (2014).

[31] D. Arnal, Three-dimensional boundary layer: laminar-turbulent transition, in: Computation of Three-Dimensional Boundary Layers Including Separation, no. 741 in 4, Agard, 1987, pp. 1 – 34 (1987).

[32] G. Bégou, Prévision de la transition laminaire-turbulent dans le code elsa par la méthode des paraboles, Ph.D. thesis, Toulouse, ISAE (2018).

[33] H. Deyhle, H. Bippes, Disturbance growth in an unstable three-dimensional boundary layer and its dependence on environmental conditions, Journal of Fluid Mechanics 316 (1996) 73–113 (1996).

[34] A. Surana, O. Grunberg, G. Haller, Exact theory of three-dimensional flow separation. Part 1. Steady separation, Journal of Fluid Mechanics 564 (2006) 57 (2006).

[35] R. Simpson, Aspects of turbulent boundary-layer separation, Progress in Aerospace Sciences 32 (5) (1996) 457–521 (1996).

[36] M. Kruse, F. Muñoz, R. Radespiel, Transition prediction results for sickle wing and NLF (1)-0416 test cases, in: 2018 AIAA Aerospace Sciences Meeting, 2018, p. 0537 (2018).

[37] R. Petzold, R. Radespiel, Transition on a wing with spanwise varying crossflow and linear stability analysis, AIAA Journal 53 (2) (2015) 321–335 (2015).

[38] M. Kruse, A. Küpper, R. Petzold, F. Munoz, Determination of the critical cross flow n-factor for the low-speed wind tunnel braunschweig (dnw-nwb), in: New Results in Numerical and Experimental Fluid Mechanics XI, Springer, 2018, pp. 251–261 (2018).

[39] D. Kim, Y. Kim, J. Li, R. V. Wilson, J. E. Martin, P. M. Carrica, Boundary layer transition models for naval applications: capabilities and limitations, Journal of Ship Research 63 (04) (2019) 294–307 (2019).